

Unraveling the Mechanisms of Ultrasound-Induced Mechanical Degradation of Microgels: Effects of Mechanoresponsive Crosslinks, Softness, and Core-Shell Architecture

Alexander V. Petrunin,^{†,‡,△} Susanne Braun,^{¶,§,△} Felix J. Byn,[‡] Indré Milvydaitė,^{¶,§} Timon Kratzenberg,[‡] Pablo Mota-Santiago,^{||,⊥} Andrea Scotti,[#] Andrij Pich,^{¶,§,©} and Walter Richtering^{*,‡}

[†]*Institute of Experimental Colloidal Physics, Heinrich-Heine University, Universitätsstr. 1, Düsseldorf, Germany*

[‡]*Institute of Physical Chemistry, RWTH Aachen University, Landoltweg 2, 52074 Aachen, Germany*

[¶]*DWI – Leibniz Institute for Interactive Materials, Forckenbeckstr. 50, 52074 Aachen, Germany, EU*

[§]*Functional and Interactive Polymers, Institute of Technical and Macromolecular Chemistry (ITMC), RWTH Aachen University, Worringerweg 2, 52074 Aachen, Germany, EU*

^{||}*Australian Synchrotron, ANSTO, Clayton, Victoria, Australia*

[⊥]*MAX IV Laboratory, Lund University, P.O. Box 118, 22100 Lund, Sweden, EU*

[#]*Division of Physical Chemistry, Lund University, SE-22100 Lund, Sweden*

[©]*Aachen Maastricht Institute for Biobased Materials (AMIBM), Maastricht University, Brightlands Chemelot Campus, Urmonderbaan 22, 6167 RD Geleen, The Netherlands, EU*

[△]*These authors contributed equally to this work.*

E-mail: richtering@pc.rwth-aachen.de

Abstract

Ultrasound-induced degradation of soft polymeric colloids, like microgels, as well as a controlled drug release enabled by mechanoresponsive bonds, has recently attracted considerable attention. However, most examples in the literature focus primarily on the applications rather than examining the underlying mechanisms of the structural changes occurring in microgels due to cavitation – changes that are crucial for developing effective drug delivery systems. In this work, we provide a comprehensive view on how microgel structure governs the susceptibility to rupture and mass loss upon cavitation, investigating both conventional microgels containing mechanoresponsive disulfide bonds and more complex asymmetrically crosslinked core-shell microgels. By combining dynamic and static light scattering, small-angle X-ray scattering, and atomic force microscopy, we demonstrate that an interplay between mechanoresponsive crosslinks and the swelling degree determines the microgels susceptibility to ultrasound-induced damage. Our findings indicate that local stress from cavitation bubbles varies strongly within the microgel dispersion. The majority of microgels undergo gradual erosion at their periphery, resulting in smaller yet structurally intact particles over time, observable by light scattering and AFM. In contrast, microgels closer to a cavitation bubble can experience partial rupture or completely disintegrate, producing smaller, more polydisperse fragments, which contributes substantially to the overall mass loss observed. In the core–shell microgels with different crosslinkers in the core and shell, degradation occurs nearly uniformly across both regions, instead of selectively targeting the weaker part. These observations highlight the complexity of the degradation dynamics as well as the similarity to processes seen in linear polymers and bulk hydrogels.

Keywords

microgels, disulfide crosslinks, ultrasound, mechanochemical degradation, light scattering, small-angle X-ray scattering, atomic force microscopy

Ultrasound treatment is widely used in medicine for diagnostic imaging, local heating or tissue ablation.¹ For imaging and most therapeutic applications, a low-intensity ultrasound in the MHz frequency range is used, which is harmless to the surrounding tissue, and its effect is limited to local heating.² Conversely, high-intensity focused ultrasonic beams offer a non-invasive but efficient stimulus to trigger drug release in desired parts of the body and promote its internalization by cells.^{3,4} This therapeutic approach, often termed sonopharmacology, relies on transforming the energy of the sound wave into a local mechanical force, similar to classical sonochemistry⁵ and polymer mechanochemistry.⁶

In contrast to most medical applications, sonochemistry uses a low-frequency (≥ 20 kHz) ultrasound of high intensity. When such ultrasound waves pass through a liquid, they induce gas bubbles (cavities) that oscillate in phase with the wave and then spontaneously implode.⁷⁻⁹ This phenomenon, known as inertial cavitation, produces huge local shear or elongational strain in the vicinity of the bubble, with strain rates on the order of 10^6 - 10^7 s⁻¹.^{10,11} Additionally, a collapsing bubble emits an intense shock wave from its center. This wave travels at supersonic speeds and can have amplitudes as high as 10^4 - 10^5 bar.¹² The mechanical forces resulting from inertial cavitation and shock waves are sufficient to break covalent bonds, destroy polymer molecules or drug carriers and release their cargo.

Designing an optimal mechanoresponsive drug carrier requires a thorough understanding of its activation/degradation process. In the case of simple linear polymers, the basics of the degradation mechanism in ultrasonication experiments are fairly well understood.^{13,14} Hence, the majority of recent research in the field of polymer mechanochemistry focuses on developing and incorporating mechanically responsive moieties – mechanophores – into polymers to achieve selective bond scission^{6,15-19} and to trigger the release of small molecules.²⁰⁻²² However, the potential mechanoresponsive drug carriers, are often significantly larger and possess a more complex structure, which can have a dramatic influence on the mechanism and efficiency of mechanical degradation.²³ Examples of such materials include polyelectrolyte multilayer capsules,²⁴ polymeric micelles,²⁵ polymerosomes,²⁶ composite hydrogels^{27,28} and

microgels.^{22,29}

Microgels, which are crosslinked polymeric colloids swollen in a good solvent, represent arguably the most versatile prototype of a polymeric drug carrier. They typically have a submicrometer size, low size polydispersity and a porous internal structure, all of which are well understood, can be easily controlled in synthesis and characterized using scattering or microscopy techniques.^{30,31} Furthermore, microgels can respond to external stimuli, like temperature,³² pH,³³ or ionic strength³⁴ by swelling and deswelling the polymer network. The extent of swelling, which is controlled by the amount of crosslinker and solvent quality,^{35,36} defines the porosity of microgels allowing to load them with small molecules,^{37,38} proteins^{39,40} or nanoparticles,^{41,42} and then release the loaded cargo on demand. Due to the soft nature of microgels,^{43–45} mechanical force can be used as an external trigger to selectively actuate or modify them, for example by ultrasound irradiation.⁴⁶

The application of a low-intensity ultrasound, especially in the MHz frequency range, does not break strong covalent crosslinks in microgels. It can induce a deswelling of pNIPAm microgels⁴⁷ or collapse of linear pNIPAm chains.⁴⁸ Another study reported an increased swelling of microgels in response to mild ultrasonic treatment.⁴⁹ Furthermore, absorption or scattering of mild ultrasonic waves by microgels can enhance the deformation of their embedding matrix, making the matrix also responsive to ultrasound.⁵⁰ In contrast, application of a high-intensity ultrasound at lower frequency (20 kHz or similar) typically leads to irreversible mechanical degradation of microgels. This effect was used in several studies to achieve on-demand release of encapsulated drugs.^{29,51–53} Notably, microgels can only be degraded in their swollen state, while collapsed microgels are resistant to degradation by ultrasound.^{51,54,55} It was also shown that incorporation of mechanophores, such as disulfide or diselenide bonds, as crosslinkers or linkers for drug molecules can significantly facilitate microgel degradation⁵⁴ or drug release,²² respectively. However, supramolecular crosslinks, such as catechin hydrogen bonds, can act as dynamic bonds and render microgels more resistant against mechanical forces.⁵⁶

The majority of the aforementioned studies showed only the proof-of-principle results that microgels can be degraded by ultrasound. Only a few works attempted to characterize the structural changes that occur in microgels as a result of cavitation. Izak-Nau *et al.* investigated poly(*N*-vinylcaprolactam) (pVCL)-based microgels that were crosslinked with a dimethacrylate-functionalized mechanofluorophore. Dynamic light scattering (DLS), cryo-transmission electron microscopy (cryo-TEM), and high-resolution magic-angle spinning nuclear magnetic resonance (HR-MAS NMR) were employed to demonstrate that the outer fuzzy shell of a microgel degrades first upon exposure to shearing forces. This results in a more homogeneous internal structure and a lower swelling degree of the microgels.⁵⁷ However, cryo-TEM may not always capture the full extent of structural changes in soft, highly-swollen particles, like microgels, because of contrast limitations. Also, DLS does not provide direct structural information as it measures the average diffusion coefficient. Alternatively, atomic force microscopy (AFM) can resolve many structural features of microgels^{44,58-62} and, therefore, is better suited to follow microgel degradation.⁴⁶ A few other studies showed cavitation-induced fragmentation of microgels into irregular debris.^{51,54} However, to the best of our knowledge, the mechanism of this fragmentation remains unknown.

Here, we investigate the mechanism and efficiency of microgel degradation by applying high-intensity ultrasound. We use dynamic light scattering (DLS), static light scattering (SLS), small-angle X-ray scattering (SAXS), and atomic force microscopy (AFM) to characterize the structural changes occurring in the microgels upon application of ultrasonication. The combination of reciprocal- and real-space techniques allows us to detect even small structural modifications and, at the same time, overcome the limitations of increasing size polydispersity.

We examine both conventional covalently crosslinked microgels and those containing mechanoresponsive disulfide crosslinks to better understand how incorporated mechanophores influence the efficiency of degradation. In addition, we investigate asymmetrically crosslinked core-shell microgels in which the disulfide crosslinks are located exclusively in either core or

shell, hypothesizing that the mechanoresponsive part (core or shell) might be selectively degraded while the other part remains intact.

The presented findings reveal that mechanical degradation of microgels by ultrasound is more complex than it was considered in previous studies,^{54,55,57} both in terms of the influence of mechanophores and the underlying mechanism.

Experimental Section

Materials

N,N'-Bis(acryloyl)cystamine (BAC, $\geq 95\%$, TCI), *N,N'*-methylenbisacrylamide (BIS, 99%, Sigma-Aldrich), ammonium persulfate (APS, $\geq 98\%$, Sigma-Aldrich), sodium dodecyl sulfate (SDS, $\geq 99\%$, Sigma-Aldrich), and tetramethylethylenediamine (TEMED, 99%, Sigma-Aldrich) were used as received and without further purification. The monomer *N*-isopropylacrylamide (NIPAm, $> 98\%$, TCI) was destabilized by recrystallization from *n*-heptane.

Syntheses

All microgels were synthesized using precipitation polymerization in deionized water. As a crosslinker either BIS or BAC were used. The reactions were monitored and optimized using an in-line reaction calorimeter. This allowed us to monitor the real-time heat generation rate and the turbidity during the reaction. For quantification of the incorporated BAC content using Raman spectroscopy, homopolymers of pNIPAm and pBAC were synthesized in deionized water. Table S1 (Supporting Information) provides internal sample codes (from lab journal) for future reference.

Synthesis of Conventional Microgels in an In-Line Reaction Calorimeter

The in-line reaction calorimeter was used to optimize the microgel polymerizations. Depending on the initiation system used, different polymerization temperatures were chosen. For APS-initiated syntheses, a polymerization temperature of 70 °C was used while for the APS/TEMED redox-initiated syntheses, a temperature of 50 °C was used. The redox-initiated synthesis was chosen in order to avoid a thermal degradation of the disulfide crosslinker BAC as reported in the literature.⁶³ In this work, we intended to keep the disulfide bond of the crosslinker intact for further degradation experiments applying ultrasound. For online monitoring of the microgel formation process, syntheses were performed

in an RC1e reactor from Mettler-Toledo (triple-walled, 0.5 L), which is equipped with a downward-facing propeller stirrer, a turbidity sensor, and two temperature sensors. For the syntheses of the microgels, NIPAm, the surfactant SDS, and the crosslinker (BIS or BAC) with varying crosslinker content (1 mol% or 5 mol%) were dissolved in deionized water. In case of the APS/TEMED-initiated microgels, TEMED was added to the mixture using a micro liter pipette. The mixture was degassed (30 min) using nitrogen, while stirred (300 rpm), and heated to the desired reaction temperature. The initiator (APS) was added in solid form. The polymerization was terminated by cooling the reactor to 25 °C after 1 to 3 hours. The temperature inside the reactor, the heat flow of the reaction as well as the turbidity were measured over the course of the whole reaction. For measurements and data analysis, the software iControl RC1e 5.3 was used. The exact amounts of chemicals used for the microgel syntheses performed in a reaction calorimeter are listed in Table S2 (Supporting Information).

Syntheses of Conventional Microgels in Round-Bottom Flask

For the synthesis of a pNIPAm microgel in a round-bottom flask, NIPAm, BAC or BIS, SDS, and TEMED (1 mol%) were dissolved in deionized water at room temperature and purged with nitrogen for 30 min. Subsequently, under constant stirring (500 rpm) the solution was heated up (50 °C) in an oil bath. To initiate the reaction, APS (1 mol%) was dissolved in deionized water (0.5 mL) and added to the reaction solution. The polymerization was terminated after 1 hour by slowly cooling down to room temperature. The molar percentage was calculated in correlation to the amount of NIPAm added. For purification of the microgel dispersion, it was dialyzed for at least 5 days against deionized water (5 L) with a cellulose membrane (MWCO 12–14 kDa). The water was exchanged at least twice a day. After purification and lyophilization, the yield was determined gravimetrically. The exact amounts of chemicals used for the synthesis of conventional pNIPAm-based microgels are listed in Table S2 (Supporting Information).

Synthesis of Core-Shell Microgels in Round-Bottom Flask

The core-shell microgels were synthesized *via* seeded precipitation polymerization in a round-bottom flask. NIPAm, TEMED, BAC or BIS, and purified core microgel solution (Tables S3 and S4, Supporting Information) were dissolved in deionized water (60 mL) at room temperature in a round-bottom flask. The dispersion was purged with nitrogen for 30 min. Subsequently, under constant stirring (500 rpm) the solution was heated (50 °C) using an oil bath. To initiate the reaction, APS was dissolved in deionized water (0.5 mL), and added to the reaction solution. The polymerization was terminated after 1 hour by slowly cooling down to room temperature. The molar percentage was calculated in correlation to the amount of NIPAm added. For purification of the microgel dispersion, it was dialyzed for at least 5 days against deionized water (5 L) with a cellulose membrane (MWCO 12–14 kDa). The water was exchanged at least twice a day. After purification and lyophilization the yield was determined gravimetrically. The exact amounts of chemicals used for the synthesis of the core-shell microgels are listed in Table S5 (Supporting Information).

Raman Spectroscopy

FT-Raman spectra were recorded with a Bruker RFS 100/S spectrometer. The samples were stimulated by a Nd:YAG laser with a wavelength of 1064 nm and an output power of 200 mW. Each sample was measured with 1000 scans and covered a spectral range from 400 to 4000 cm^{-1} with a resolution of 4 cm^{-1} . The baseline correction and the analysis of the recorded spectra were carried out with the software OPUS 4.0.

The quantification of the BAC content within the microgels was performed using calibration curves. Therefore, pNIPAm and pBAC were mixed in specific ratios and homogenized by dissolving both in methanol. The solvent was removed by evaporation at room temperature, and the solid samples were measured to obtain a calibration curve.

Ultrasonication Experiments

Sonochemical irradiation experiments were performed under an inert atmosphere on a Vibra-Cell ultrasonic processor VCX500 (Sonics & Materials) in a three-neck Suslick vessel (Zinsser Analytic). For each degradation experiment, the pristine microgels were diluted (0.5 mg mL^{-1}), filled into the Suslick vessel, which was sealed with septa, placed in an ice bath, and then degassed with nitrogen for 10 min. The microgel dispersions were sonicated with a 13 mm probe (maximum displacement amplitude of $A_{\max} = 115 \mu\text{m}$) for different periods of time between 5 and 180 min in a pulsed ultrasonication mode (1 s “on” and 2 s “off”, i.e. 33% duty cycle). The frequency was $f = 20 \text{ kHz}$, and the amplitude was kept at 30%. These settings correspond to the nominal ultrasound intensity of $I_{\text{nom}} = 2\pi^2 f^2 A^2 \rho c \approx 1.5 \cdot 10^8 \text{ W/m}^2$ and nominal acoustic pressure of $P_{\text{nom}} = 2\pi f A \rho c \approx 64 \text{ bar}$.¹⁴

Dynamic and Static Light Scattering

Multi-angle dynamic light scattering (DLS) was used to determine the hydrodynamic radius of the microgels, R_h . The measurements were performed using an ALV instrument equipped with a HeNe laser (wavelength in vacuum $\lambda_0 = 633 \text{ nm}$) and a digital correlator. The measurements were performed at $T = 20 \text{ }^\circ\text{C}$ in double-distilled water (refractive index $n(\lambda_0) = 1.332$) filtered through a $0.2 \mu\text{m}$ syringe filter. The temperature was controlled using a toluene bath to match the refractive index of the glass vial and an external bath circulator. The scattering intensity was measured at scattering vectors $q = 4\pi n / \lambda_0 \sin \theta / 2$, where the scattering angle θ was changed between 30° to 110° degrees in 5° or 10° steps. The time of acquisition was 60 s per angle.

Static light scattering (SLS) measurements were performed in double-distilled water filtered through a $0.2 \mu\text{m}$ syringe filter using an SLS-Systemtechnik GmbH instrument equipped with a blue laser ($\lambda_0 = 407 \text{ nm}$), a far-red laser ($\lambda_0 = 819 \text{ nm}$) and an index-matched toluene bath. The scattering intensity was measured at $T = 20 \text{ }^\circ\text{C}$ as a function of the scattering vector q by changing the scattering angle θ between 20° and 150° with a 2° step.

Small-Angle X-Ray Scattering

The small-angle X-ray scattering (SAXS) experiments were performed at the CoSAXS beamline at the 3 GeV synchrotron ring of the MAX-IV Laboratory (Lund, Sweden).⁶⁴ The q -range between $1 \cdot 10^{-2}$ and 0.7 nm^{-1} was covered on the CoSAXS using a sample-to-detector distance of 10 m and the X-ray beam energy of $E = 12.4 \text{ keV}$. The Eiger2 4M SAXS detector with pixel size of $75 \mu\text{m} \times 75 \mu\text{m}$ was used. The data were reduced using the Python scripts used at the beamline.

The scattering intensity $I(q)$ was fitted with the form factor model of a fuzzy-sphere for regular microgels⁶⁵ (SAXS data) and a fuzzy core-shell for the core-shell microgels^{66,67} (SLS data) using a custom Matlab-based software *FitIt!*⁶⁸ In the fuzzy-sphere form factor model, it is assumed that a particle of radius R consists of a homogeneous core of radius R_c and a fuzzy shell of width 2σ , such that $R = R_c + 2\sigma$. In the fuzzy core-shell form factor model, a particle of radius R is assumed to have a homogeneous core of radius R_c , an interpenetrating layer between the core and the shell of the length $2\sigma_{\text{in}}$, a homogeneous shell of length w and a fuzzy outer surface of the length $2\sigma_{\text{out}}$. The total particle radius is given by a sum of the above parts, $R = R_c + 2\sigma_{\text{in}} + w + 2\sigma_{\text{out}}$. The size polydispersity in both models is accounted for by convolving the form factor with a Gaussian distribution of the total radius R .^{65,66} An additional Lorentzian term with an average mesh size ξ can be added to account for scattering from density inhomogeneities of the polymer network at high q -values (irrelevant for SLS data).^{32,65}

Atomic Force Microscopy

The samples for dry-state atomic force microscopy (AFM) measurements were prepared *via* dip coating on silicon substrates (ca. 1.5x1.5 cm). The substrates were cleaned in isopropanol using an ultrasound bath and activated using a UV Ozone Cleaner (NanoBioAnalytics UVC-1014) prior to deposition. The microgel dispersions at a concentration of 3.5 mg mL^{-1} were mixed with isopropanol in a 1:4 ratio (v/v), and between 30 and 120 μL of the mixture was

deposited on a custom glass trough filled with Milli-Q water (surface area $A_{\text{tot}} = 50.27 \text{ cm}^2$). The substrates were lifted out of the trough at a speed of 0.67 mm s^{-1} following 25 minutes of equilibration.

The AFM images were recorded using a Nanosurf NaioAFM instrument and a BudgetSensors TAP190Al-G probe (cantilever) with a spring constant of 48 N m^{-1} , a resonant frequency of 190 kHz and a nominal tip radius of 10 nm. The tapping mode of the instrument was used with a vibrational amplitude of $\approx 230 \text{ mV}$. The AFM images were corrected using the Gwyddion software (version 2.61).⁶⁹ A custom Matlab script (MathWorks, 2022b) was employed for the measurement of the contact radii R_{cont} and the AFM height profiles. The script automatically detects the microgel centers based on the height image data and assigns a region of interest (ROI) to the corresponding phase image. The ROI is then manually adjusted to measure R_{cont} assuming a circular geometry of the individual microgels spread at the interface. The microgel detection is based on the particle tracking algorithm described by Crocker *et al.*^{59,70} For each microgel, two height profiles are generated by linear interpolation of the height data around the microgel center parallel and orthogonal to the fast scan direction of the AFM image, respectively.

For each microgel sample corresponding to a different ultrasonication time t , between 5 and 16 AFM images were recorded, so that between 52 and 403 individual microgels were analyzed by the script. The statistical analysis was performed with the one-way ANOVA test and Tukey-Kramer post-hoc pairwise comparison using built-in functions in Matlab (MathWorks, 2022b): *anova1* and *multcompare*, significance level 0.05.

Results

Microgel Synthesis and Ultrasonication

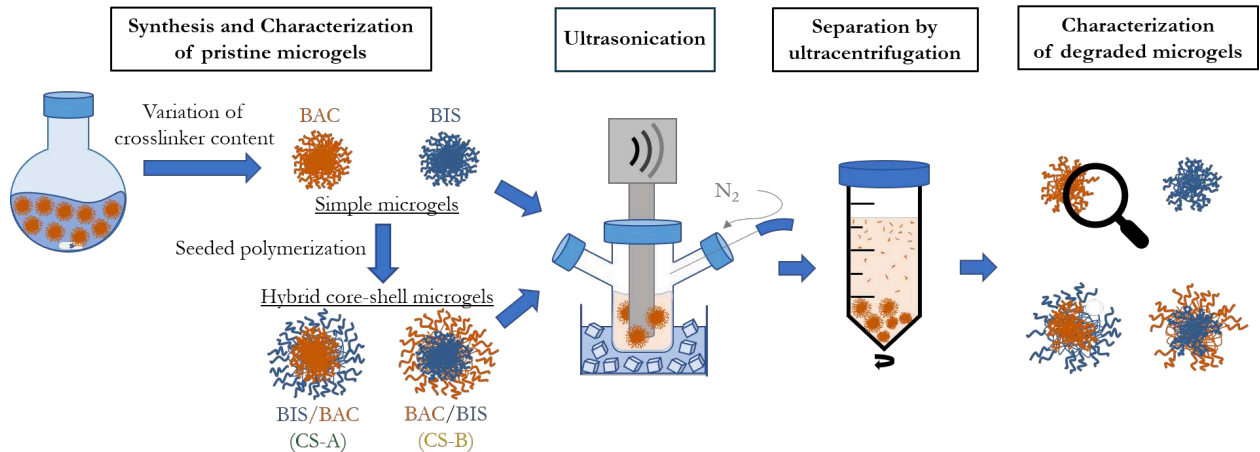
The microgels used in this study were synthesized by precipitation polymerization of *N*-isopropylacrylamide (NIPAm) in demineralized water⁷¹ using either a conventional cross-linker *N,N'*-methylenebisacrylamide (BIS) or a mechanoresponsive disulfide crosslinker *N,N'*-bis(acryloyl)cystamine (BAC). The microgels containing a single type of crosslinker and synthesized in a single polymerization step will be referred to as *conventional* microgels, Table 1. Additionally, asymmetrically crosslinked *core-shell* microgels were synthesized with a different crosslinker in the core and shell using a seeded precipitation polymerization with the conventional microgels acting as seeds.⁷² The hydrodynamic radii, R_h , of all the obtained microgels in the swollen state ($T = 20$ °C, below the VPT temperature) and in the collapsed state ($T = 40$ °C, above the VPT temperature) are shown in Table 1. We calculate the swelling ratio of the microgels as the quotient of the swollen and collapsed hydrodynamic radius, $\alpha = R_h(20\text{ }^\circ\text{C})/R_h(40\text{ }^\circ\text{C})$. The swelling ratio is used as a measure of the softness of a microgel – the higher the swelling ratio, the softer the microgel.⁴⁵ Microgels with a higher amount of crosslinker (5 mol% *vs.* 1 mol%) have a lower swelling ratio making them effectively harder, as expected,⁷³ Table 1. Interestingly, the microgels with BAC crosslinker have smaller values of α than the microgels with the same nominal amount of BIS crosslinker. This observation is unexpected but it can be explained by a significantly higher hydrophobicity of the BAC molecules, as well as by side-reactions of the BAC crosslinker that might occur during the synthesis.⁶³ A detailed discussion of the difference in swelling of the microgels, supported by in-line reaction calorimetry and Raman spectroscopy data, is given in Sections S2-S4 and Figures S1-S3 (Supporting Information).

Mechanical degradation of the microgels was achieved by irradiating them under a nitrogen atmosphere with 20 kHz ultrasound using a sonotrode, Scheme 1. An ice bath was used to prevent the heating of the irradiated samples and to ensure that the microgels remained

Table 1: Characteristics of the investigated microgels, including their hydrodynamic radii in swollen state $R_h(20\text{ }^\circ\text{C})$, in the collapsed state $R_h(40\text{ }^\circ\text{C})$, and the swelling ratios α .

Name	Type of microgel	Crosslinker (core/shell)	$R_h(20\text{ }^\circ\text{C})$ [nm]	$R_h(40\text{ }^\circ\text{C})$ [nm]	α
BIS-1	conventional	1 mol% BIS	142 ± 2	50.5 ± 0.4	2.82 ± 0.05
BIS-5	conventional	5 mol% BIS	140 ± 3	66.1 ± 0.5	2.11 ± 0.04
BAC-1	conventional	1 mol% BAC	127.7 ± 0.7	66.4 ± 0.5	1.92 ± 0.02
BAC-5	conventional	5 mol% BAC	103.3 ± 0.5	69.0 ± 0.8	1.50 ± 0.02
CS-A	core-shell	1 mol% BAC/1 mol% BIS	380 ± 8	156 ± 2	2.44 ± 0.06
CS-B	core-shell	1 mol% BIS/1 mol% BAC	318 ± 12	151 ± 3	2.11 ± 0.09

in the swollen state. After the ultrasonication, any cleaved polymer chains and network fragments were removed by centrifugation at 50,000 rpm and only the purified microgels were analyzed further. We performed a trial DLS measurement of the supernatant, which showed that the intermediate scattering function, $f(q, \tau)$, did not follow a single-exponential course, and the obtained decay rates, $\Gamma(q)$, did not strictly obey the q^2 scaling. Therefore, a light scattering characterization of the supernatant requires its separation into relatively monodisperse fractions, which is out of the scope of this manuscript and will be addressed in a separate study.



Scheme 1: Schematic of the experimental approach used in this study: after ultrasonication, microgels are separated from any cleaved chains and fragments by ultracentrifugation and then analyzed using various scattering methods and atomic force microscopy.

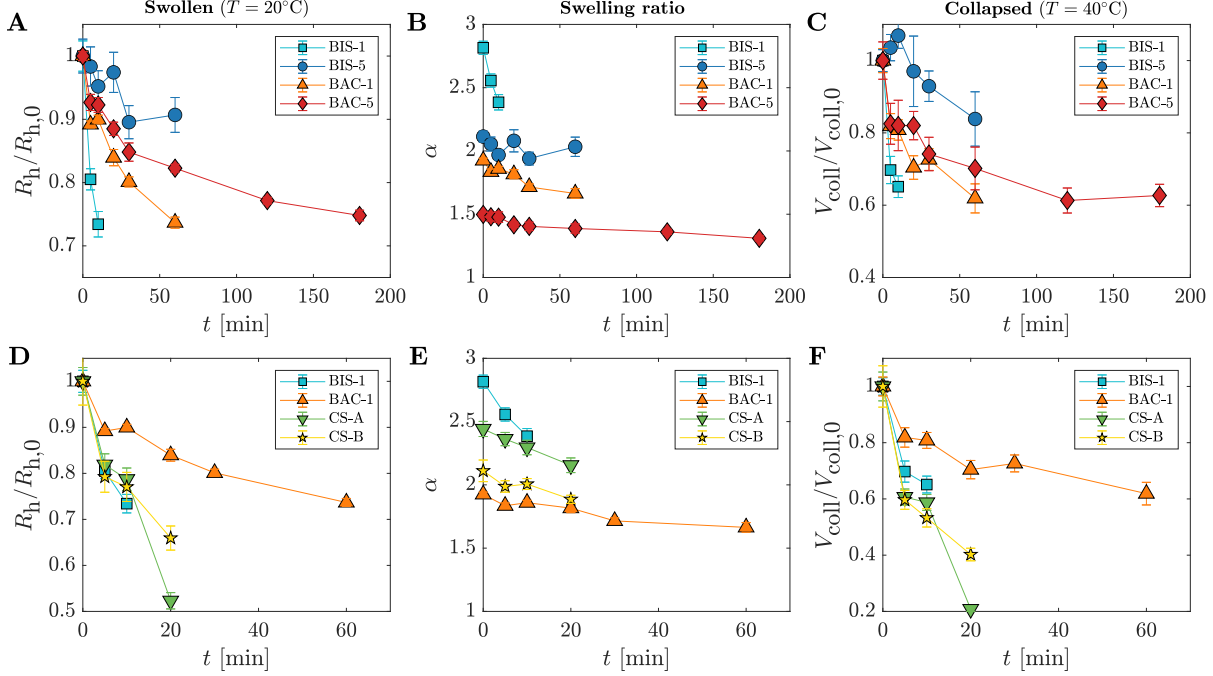


Figure 1: (A,D) Normalized hydrodynamic radii of the conventional microgels (A) and core-shell microgels (D) in the swollen state ($T = 20^\circ\text{C}$), $R_h/R_{h,0}$, after different ultrasonication times t . (B,E) Swelling ratio α of the conventional microgels (B) and core-shell microgels (E) after different ultrasonication times t . (C,F) Normalized volume of the conventional microgels (C) and core-shell microgels (F) in the collapsed state ($T = 40^\circ\text{C}$), $V_{\text{coll}}/V_{\text{coll},0}$, after different ultrasonication times t .

Degradation of Microgels Observed by DLS

First, we measure the decrease of the microgel size due to the ultrasonic irradiation using DLS. This is commonly done in the literature to assess the stability of microgels against mechanical degradation.^{22,54-57} Figure 1A shows the hydrodynamic radii of the microgels measured by multi-angle DLS at $T = 20^\circ\text{C}$ after different ultrasonication times t , normalized by the hydrodynamic radius of the pristine microgels, $R_{h,0}$. The radii of microgels in the collapsed state ($T = 40^\circ\text{C}$) are shown in Figure S5A and their change with t is qualitatively similar. The hydrodynamic radii decrease gradually for all microgels but the rate of the decrease depends significantly on the amount and type of crosslinker. Generally, microgels with fewer crosslinks degrade faster, for example BIS-1 (cyan squares) *vs.* BIS-5 (blue circles) or BAC-1 (orange triangles) *vs.* BAC-5 (red diamonds), in agreement with other studies.^{56,57}

When comparing BIS-5 (blue circles) and BAC-5 microgels (red diamonds), it can be seen that the presence of mechanoresponsive bonds makes the microgels more degradable by ultrasound, also as expected.⁵⁴ In contrast, a comparison of BIS-1 microgels (light blue squares) and BAC-1 microgels (orange triangles) gives the opposite result: in this case BIS microgels are more susceptible to mechanical degradation. To reconcile this discrepancy, we consider that BAC and BIS microgels have a different swelling degree, α , Table 1: BIS-1 microgels have a lower value of α than BAC-1 microgels. Indeed, strong swelling is known to introduce internal stresses in polymer materials making them more susceptible to mechanical failure.⁷⁴ The effect of swelling dominates over the effect of the labile (disulfide) bonds for BIS-1 *vs.* BAC-1 microgels. The difference in swelling might also contribute to the small difference in mechanical stability between BAC-5 and BIS-5 microgels. Therefore, the resistance of microgels to mechanical degradation results from a complex interplay between the presence of mechanoresponsive bonds, the amount of crosslinker and the swelling degree. Over the course of ultrasonic degradation, the swelling degree of all microgels decreases in agreement with previous work,⁵⁷ Figure 1B. This indicates that microgels should become more mechanically-resistant and degrade slower over time, which is in line with the data in Figure 1A.

The extent of degradation of the microgels can be quantified by their relative mass loss: the decrease of the molecular weight M_w . Since the size of a microgel in the collapsed state does not depend on the degree of crosslinking or internal structure,³⁵ the volume of a collapsed microgel obtained by DLS, V_{coll} , provides a good measure of its molecular weight, M_w :

$$M_w \propto V_{\text{coll}} = \frac{4}{3}\pi R_h^3(40 \text{ }^{\circ}\text{C}). \quad (1)$$

Figure 1C shows the course of the normalized volume of a collapsed microgel $V_{\text{coll}}/V_{\text{coll},0}$ with increasing ultrasonication time. The data for all microgels do not follow a linear trend, indicating that degradation becomes slower with increasing t . Surprisingly, the value of $V_{\text{coll}}/V_{\text{coll},0}$ for BAC-5 microgels tends to a plateau at $t > 100$ min. In addition, BIS-1 micro-

gels after 10 min and BAC-1 microgels after 60 min showed a very low scattering intensity (not shown), such that sufficiently good data could not be obtained at larger ultrasonication times for these microgels. Yet, the relative decrease of molecular weight (collapsed volume) is unexpectedly small, less than 40%.

Further unexpected observations can be found in the DLS data for the core-shell microgels. Figure 1D shows the normalized hydrodynamic radii *vs.* ultrasonication time t for the microgels with BAC crosslinker in the core and BIS in the shell, CS-A (green downward triangles), and *vice versa* BIS in the core and BAC in the shell, CS-B (yellow stars). Because of the presence of both BIS and BAC crosslinkers, as well as intermediate swelling degree (Table 1 and Figure 1E), the core-shell microgels are expected to have a stability intermediate between the two conventional microgels with the same amount of crosslinker: BIS-1 (cyan squares) and BAC-1 (orange downward triangles). Yet, both CS-A and CS-B decrease their relative hydrodynamic radius approximately as fast as BIS-1 microgels. The relative molecular weight (collapsed volume) of the core-shell microgels decreases even faster than for BIS-1 microgels, Figure 1F. These observations indicate that the microgel degradation cannot be understood based solely on DLS data, but a more detailed structural characterization is needed.

Structural Changes of Microgels Observed by Static Scattering

The changes to the internal structure of microgels as a result of their mechanical degradation were first investigated using static scattering methods: SLS and SAXS. These methods provide ensemble-average information and, because of the low polydispersity of the studied microgels, are highly sensitive to small structural changes. SLS is used for the conventional BIS- or BAC-crosslinked microgels to gain a model-free structural information at the length scale of the whole particle (low values of the scattering vector q). To fit the data, we use the Guinier approximation:⁷⁵

$$\ln I(q) = \ln I_0 - \frac{R_g^2}{3}q^2, \quad (2)$$

where I_0 is the forward scattering intensity and R_g the average radius of gyration – a measure of radial distribution of mass in a particle. This effective radius is always smaller than R_h , as shown schematically in Figure 2A. Figure 2B shows the examples of Guinier plots, $\ln I(q)$ *vs.* q^2 , along with fits (black solid lines) for BAC-1 microgels with increasing ultrasonication time (from bottom to top). SLS data for other microgels and the R_g values obtained from the fits are shown in Figure S6 and Figure S7 (Supporting Information). The R_g values also decrease with increasing sonication time t for all microgels, but slower compared to R_h values. We can quantify this difference by calculating the quotient of the radius of gyration and hydrodynamic radius, $\rho = R_g/R_h$. This value is a sensitive structural parameter related to the fuzziness of a particle.^{76–79} Figure 2C shows the ρ -parameter *vs.* t for the investigated conventional microgels. Before ultrasonic degradation, $\rho \approx 0.6 – 0.65$ for all studied microgels, which is compatible with a fuzzy sphere structure of pNIPAm microgels.^{76,79} With increasing ultrasonication time, ρ gradually increases and this increase proceeds faster for less mechanically stable microgels. The increase of the structural parameter ρ can be explained by removal of the dangling or loosely-crosslinked polymer chains at the microgel periphery, as discussed in previous studies.^{54,56,57} Nevertheless, within the investigated ultrasonication times the values of ρ only reach the limit of homogeneous spheres, $\rho_{HS} = 0.778$ ⁷⁶ (Figure 2C, dashed line), for BIS-1 microgels, which are the weakest. We note that at this point the scattering signal is quite low for BIS-1 microgels and the resulting R_h is prone to error. All other microgels do not reach the homogeneous-sphere limit, which means they retain a fuzzy structure to some extent for the whole duration of the ultrasound application. Thus, the structural parameter ρ allows quantifying the loss of dangling chains in the microgel periphery during ultrasonication that has only been qualitatively reported so far.⁵⁷

Next, we perform SAXS measurements of the microgels in dilute suspension ($T = 20$ °C, swollen state) before and after ultrasonic degradation. This allows us to analyze changes in the full form factor $P(q)$ of the microgels, which describes their internal structure, by fitting the data to an appropriate model. Figure 2D shows the SAXS intensities of BAC-1

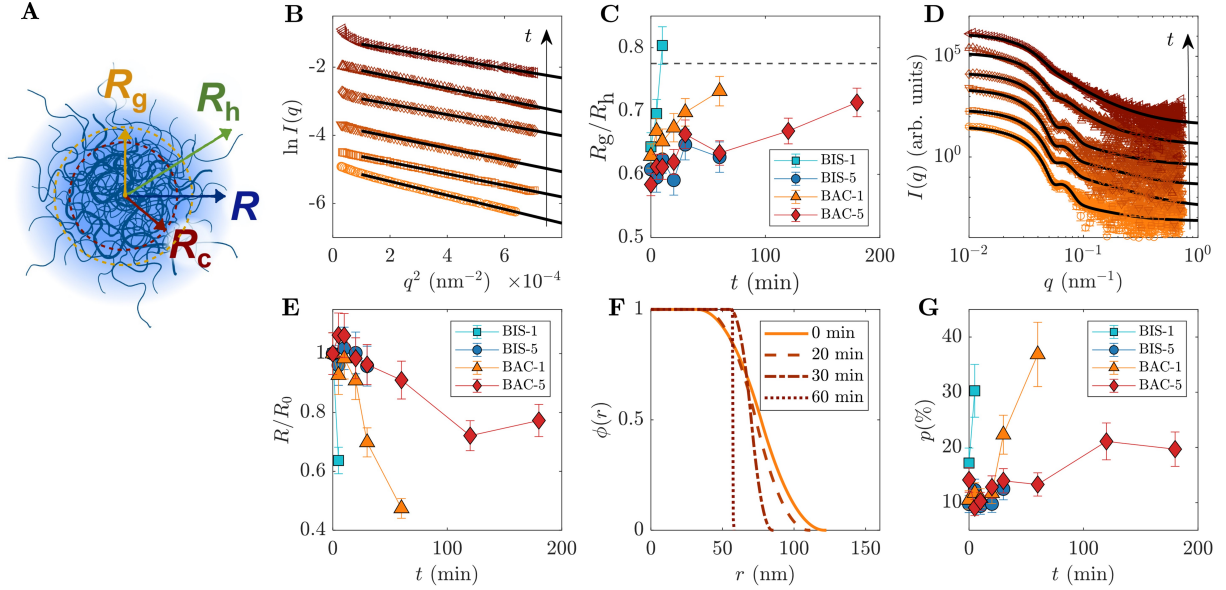


Figure 2: (A) Schematic of the different parameters describing microgel size and internal structure: the hydrodynamic radius R_h , the radius of gyration R_g , the total radius R and radius of the core R_c from the form factor fits. (B) Guinier plots of SLS intensity, $\ln I(q)$ vs. scattering vector q , for BAC-1 microgels after 0 min, 5 min, 10 min, 20 min, 30 min and 60 min ultrasonication (from bottom to top). Black lines correspond to the fits with Equation 2. (C) The R_g/R_h ratios for microgels vs. ultrasonication time t . The dashed line correspond to the value for hard spheres, $R_g/R_h = 0.778$. (D) SAXS intensities $I(q)$ vs. scattering vector q for BAC-1 microgels after 0 min, 5 min, 10 min, 20 min, 30 min and 60 min ultrasonication (from bottom to top). Black lines correspond to the fits using the fuzzy-sphere model. (E) Normalized radii of the microgels R/R_0 obtained from the SAXS fits vs. t . (F) Radial profiles of relative polymer density, $\phi(r)$, for BAC-1 microgels, obtained from the SAXS fits. (G) Polydispersities of the microgels p , obtained from the SAXS fits vs. t .

microgels with increasing ultrasonication times (from bottom to top). The shoulder at $q \sim 7 \cdot 10^{-2} \text{ nm}^{-1}$ shifts slightly to higher q -values and the minima become more smeared with increasing ultrasonication time t . The data for other microgels are shown in Figure S8 (Supporting Information). The scattering intensities are fitted with the form factor model of a fuzzy sphere, which has been shown to accurately describe the internal structure of pNIPAm microgels,^{65,80,81} Figure 2D (black solid lines). The model provides the following parameters that describe the fuzzy-sphere structure: the total microgel radius R , the radius of the highly-crosslinked core R_c , the width of the fuzzy shell 2σ , and the size polydispersity p . All the obtained fit parameters are given in Table S8 (Supporting Information). The

radii of microgels R after different ultrasonication times, normalized by the value before ultrasonication R_0 , are shown in Figure 2E. In contrast to the hydrodynamic radii R_h , the determined R corresponds to the entire crosslinked network of a microgel including both core and fuzzy shell, but it excludes the dangling chains at the microgel periphery.⁷⁶ The difference between R and R_h is shown schematically in Figure 2A.

In the first 20 min of ultrasonication, the R/R_0 values remain almost constant and close to 1 for all microgels except the BIS-1. This is in stark contrast to the $R_h/R_{h,0}$ values from DLS and the ρ -parameter from SLS/DLS, which both experience the strongest change within the first 20-30 min. Therefore, we can conclude that during the initial degradation period only very loose dangling chains (visible mostly in DLS) are removed from the microgels, whereas most of the polymer network (visible in SAXS) remains relatively intact. Here, the BIS-1 microgels are an exception: they are completely degraded within 20 min under the experimental conditions because of their extreme softness. The fuzziness of the microgels also hardly changes during the initial degradation period. This is shown in Figure 2F for BAC-1 microgels using the radial distributions of relative polymer density, $\phi(r)$, obtained from the fits: solid line (0 min) *vs.* dashed line (20 min). Despite the decrease of R_h and increase of the ρ -parameter, microgels remain fuzzy and retain most of their shell.

After a certain “critical” ultrasonication time, which depends on the mechanical stability of the microgels, the polydispersity obtained from the SAXS fits p increases dramatically, Figure 2G. For BIS-1 microgels this happens already after 5 min of ultrasonication, for BAC-1 microgels after 30 min and for BAC-5 microgels after 120 min. The increase of polydispersity means that microgel degradation proceeds non-uniformly resulting in a broad distribution of particle sizes or shapes. Interestingly, the increase of polydispersity p coincides with the strong decrease of the radii from the fit, R/R_0 . This means that removal of large parts of the polymer network inevitably leads to heterogeneous particles. During this late degradation period, the fuzziness of BAC-1 microgels decreases and the microgels eventually become homogeneous, Figure 2F (dashed-dotted and dotted lines). However, the

large polydispersity at 30 and 60 min ($p > 20\%$) smears the data significantly, so the size and internal structure extracted from these fits are subject to large uncertainties and should be treated with caution. In contrast, BAC-5 microgels, which are more resistant to mechanical degradation, remain fuzzy even after 180 min ultrasonication, Figure S8C and Table S8 (Supporting Information). When microgels are completely degraded, the SAXS scattering profiles become featureless, and a unique meaningful fit is not possible, see Figure S8A (Supporting Information). It is important to note that the samples investigated by SAXS were first purified by ultracentrifugation. This preparatory step most likely removed many of the smaller fragments formed during the ultrasonic treatment. As a result, the measured fraction contains mostly larger, relatively uniform particles. This has a particularly significant impact on the reported values for polydispersity, which may not fully capture the true extent of degradation-induced heterogeneity.

Since the BIS-1 microgels are degraded faster than BAC-1 microgels, we hypothesized that in the core-shell microgels, CS-A and CS-B, the “weaker” part (core or shell, crosslinked with BIS) is degraded first, followed by the “stronger” part (shell or core, crosslinked with BAC, respectively). To check our hypothesis, we measured the form factors of CS-A and CS-B microgels after different ultrasonication times using SLS. SLS was chosen due to the low q -range needed for the larger size of the core-shell microgels. Figures 3A and 3B show the SLS form factors of CS-A and CS-B microgels, respectively, with increasing t (from bottom to top). Black lines show the fits using the fuzzy core-shell model,⁶⁶ which takes into account the different polymer density in the core and shell because of the different crosslinkers. All fit parameters are shown in Table S9 (Supporting Information). Figure 3C shows the normalized radii of the core-shell microgels, R/R_0 , obtained from the fits. Similar to the conventional microgels, R/R_0 decrease slower than the normalized hydrodynamic radii, $R_h/R_{h,0}$, because the dangling chains are removed faster than the more densely crosslinked parts of the microgel network. Figure 3D shows the relative polymer density $\phi(r)$ after different t , which reflects the structural changes of CS-A microgels. In the pristine state, the shell

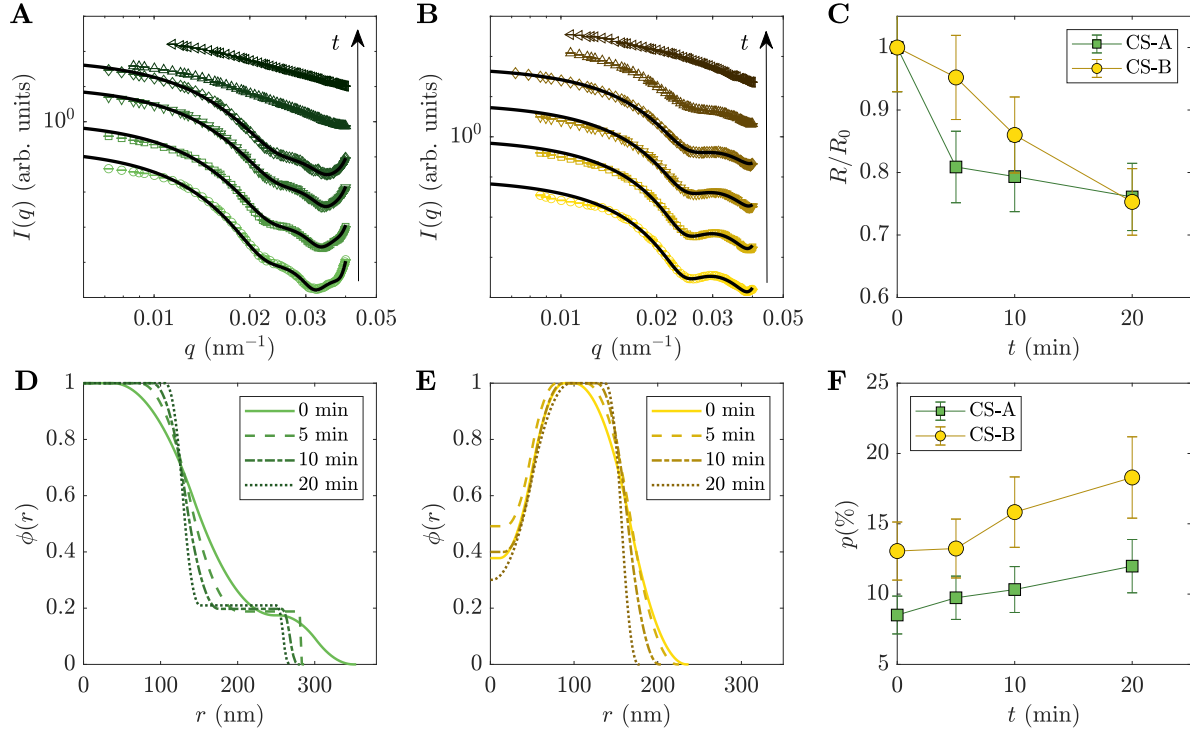


Figure 3: **(A)** SLS intensities $I(q)$ vs. q for CS-A microgels after 0 min, 5 min, 10 min, 20 min, 30 min and 60 min ultrasonication (from bottom to top). Black lines correspond to the fits using the fuzzy core-shell model. **(B)** SLS intensities $I(q)$ vs. q for CS-B microgels after 0 min, 5 min, 10 min, 20 min, 30 min and 60 min ultrasonication (from bottom to top). Black lines correspond to the fits using the fuzzy core-shell model. **(C)** Normalized radii of the core-shell microgels R/R_0 obtained from the SLS fits vs. t . **(D)** Radial profiles of relative polymer density for CS-A microgels, $\phi(r)$, obtained from the SLS fits. **(E)** Radial profiles of relative polymer density for CS-B microgels, $\phi(r)$, obtained from the SLS fits. **(F)** Polydispersities of the core-shell microgels, p , obtained from the SLS fits vs. t .

crosslinked with BIS is more swollen (has lower polymer density) than the core crosslinked with BAC. Considering the different resistance of the conventional BIS-1 and BAC-1 microgels to ultrasonic degradation (see Figure 1), one would expect the BIS-crosslinked shell of the CS-A microgels to be removed first followed by degradation of the BAC-crosslinked core. However, this is not the case, and the core-shell structure persists up to the late stages of degradation (20 min), Figure 3D (dotted line). The fuzziness of the CS-A microgels decreases with increasing t similar to the conventional microgels, but only the very periphery of the microgel is affected. Furthermore, the relative polymer density $\phi(r)$ in the shell (plateau at $r \approx 200 - 250$ nm) remains the same relative to the core. This means that the shell and the

core either degrade simultaneously or not degrade at all.

The CS-B microgels have an inverted structure with respect to the CS-A microgels: the shell crosslinked with BAC is less swollen than the core crosslinked with BIS, Figure 3E (solid line). This core-shell structure is also preserved during ultrasonication and only the very periphery is degraded, Figure 3D (dashed and dotted lines). So contrary to our initial hypothesis, the more degradable part (core or shell) of a core-shell microgel is not removed selectively by the mechanical force. Instead, the whole core-shell microgel is affected. At the same time, the polydispersity also gradually increases with t , Figure 3F. At the very late stages of degradation ($t > 20$ min), Figures 3A and 3C (upward and left triangles), the scattering profiles become featureless because of high polydispersity. In this case, the data cannot be fitted unambiguously.

Atomic Force Microscopy

As suggested by the SAXS and SLS results, an extensive ultrasonic degradation of microgels eventually leads to non-uniform particles with a broad distribution of sizes or shapes. Although scattering methods are perfectly suited to determine ensemble average properties, the exact structural changes in each particle leading to the observed non-uniformity are masked by the averaging. Therefore, we performed Atomic Force Microscopy (AFM) to follow the degradation on the single-particle level. The microgels were deposited on silicon substrates and imaged in dry state. First, we focus on BAC-1 and BIS-5 microgels as examples of microgels that are moderately resistant and highly resistant to ultrasonication, respectively.

Figure 4A-D shows example AFM images for BAC-1 microgels after various ultrasonication times: height images (top row) and phase images (bottom row). The microgels flatten at the interface and show a typical core-corona structure.⁵⁹ In the height images, only the core is observed, while the phase images also resolve the thin corona, which appears as light circles surrounding the core. The inset of Figure 4A shows a magnified image of a microgel with the core-corona structure. The white dashed circle shows the radius of the corona that

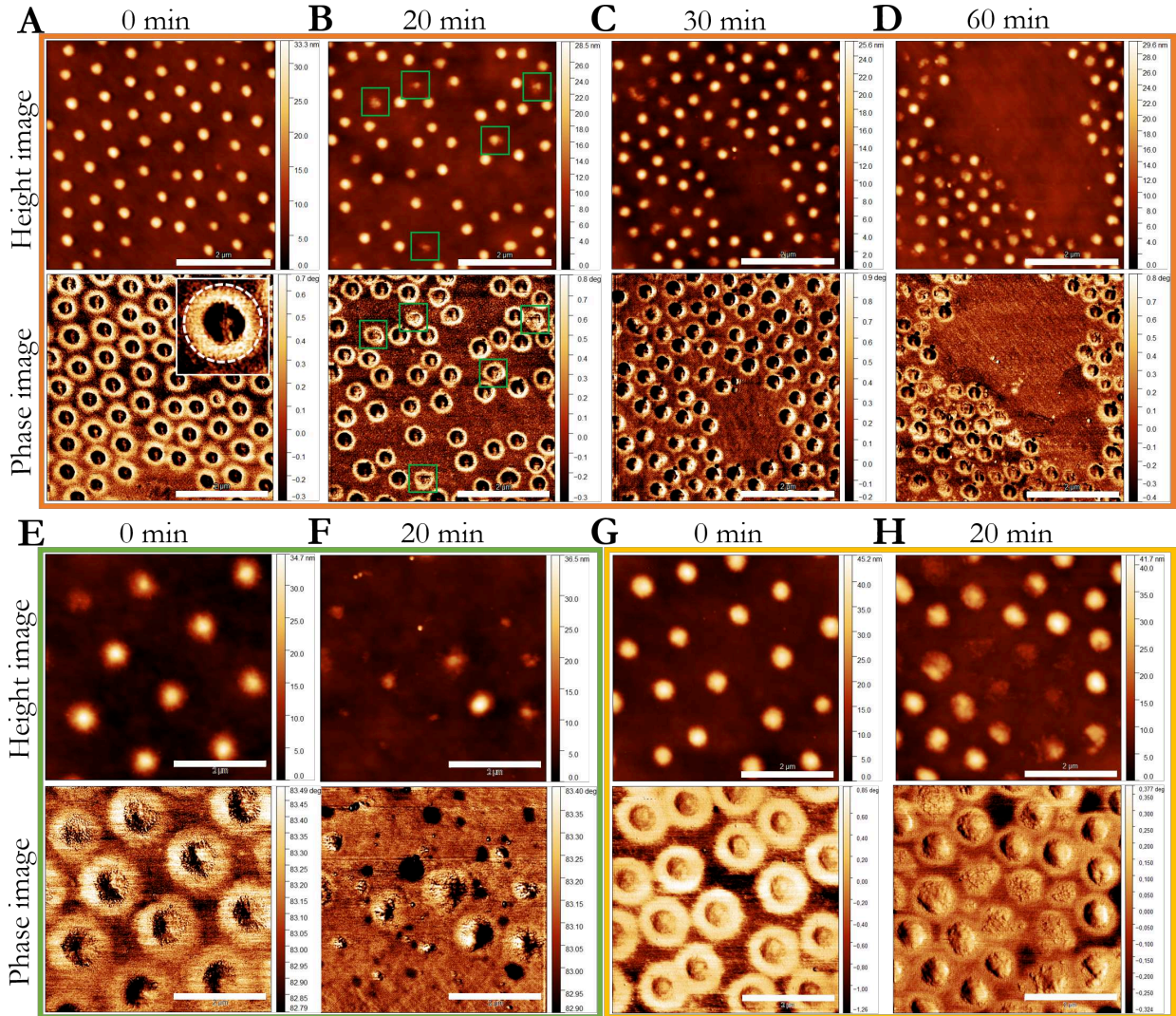


Figure 4: Examples of AFM images of BAC-1 microgels (**A-D**), CS-A microgels (**E,F**), and CS-B microgels (**G,H**) after different ultrasonication times (indicated in the figure). Upper images in each panel are height images, and lower images are phase images. Scale bars are $2 \mu\text{m}$. Inset in panel **A** (phase image) shows an enlarged microgel and its contact radius R_{cont} (white dashed circle). Green squares in panel **B** highlight ruptured microgels.

is known as the *contact radius*, R_{cont} .

Only whole microgels and no small fragments or linear chains can be seen in the images. This indicates that any fragments produced due to microgel degradation are successfully removed during the centrifugation step. Before ultrasonication, the microgels are monodisperse and radially symmetric, Figure 4A. However, after 20 min of ultrasonic degradation several irregularly-shaped microgels are observed in the height and phase images, Figure 4B

(highlighted with green squares). At the same time, the rest of the microgels are much less affected by ultrasonication: they remain symmetric and have similar heights as pristine ones. With increasing ultrasonication time, more of the irregularly-shaped microgels can be seen in the AFM images, Figure 4C (30 min) and Figure 4D (60 min). Remarkably, even highly degraded microgels retain the corona in the phase images. BIS-5 microgels are affected by ultrasonication in a similar fashion but to a lesser extent, with fewer asymmetric microgels visible in the images, Figure S9 (Supporting Information).

We propose that the irregular shapes of the microgels are a result of a partial rupture of their network followed by adsorption at the substrate interface. Strong mechanical forces caused by cavitation can create cracks or weak points in the polymer network. Upon adsorption, the microgels are further broken by surface forces resulting in highly irregular shapes. The rupture of microgels is also the most likely reason for the apparent increase of polydispersity after long ultrasonication times, Figure 2G.

Next, we probe the asymmetrically crosslinked core-shell microgels using AFM. Figure 4E and 4F show examples AFM images of CS-A microgels before and after 20 min ultrasonication, respectively. Similarly to the conventional microgels, mechanical degradation caused by the ultrasonication transforms the core-shell microgels into a mixture of irregularly-shaped (ruptured) and relatively intact particles. In agreement with the SLS data (Figure 3D and 3E), selective degradation of the shell or core is not observed. Compared to the conventional BAC-1 and BIS-5 microgels, the ruptured microgels predominate in the image and also appear much smaller and more irregular in size and shape. Similarly, the CS-B sample after 20 min ultrasonication shows many irregularly-shaped particles, Figure 4H *vs.* Figure 4G (before ultrasonication). Compared to the CS-A microgels, the ruptured CS-B microgels assume a more flat “pancake-like” morphology with an asymmetric shape. The difference in the shape of ruptured CS-A and CS-B microgels may be related to preferential rupturing in the shell or core, respectively, and should be the subject of a follow-up study. The larger fraction of ruptured particles in the AFM images of both CS-A and CS-B microgels com-

pared to the conventional microgels can be explained as follows. The core-shell microgels are larger than the conventional microgels (Table 1), so their ruptured fragments are also larger and, therefore, less likely to be removed during the centrifugation step, see Scheme 1. The presence of these fragments explains why in DLS the core-shell microgels appear to degrade faster than BIS-1 microgels, contrary to the initial expectation (Figure 1D and 1F). The intermediate scattering function, $f(q, \tau)$, follows a single-exponential rather than a double-exponential course, which means that the diffusion coefficient of the fragments is not \gg than that of the whole microgels. Consequently, the apparent R_h values for CS-A and CS-B are the average between the hydrodynamic radii of the whole microgels and the fragments.

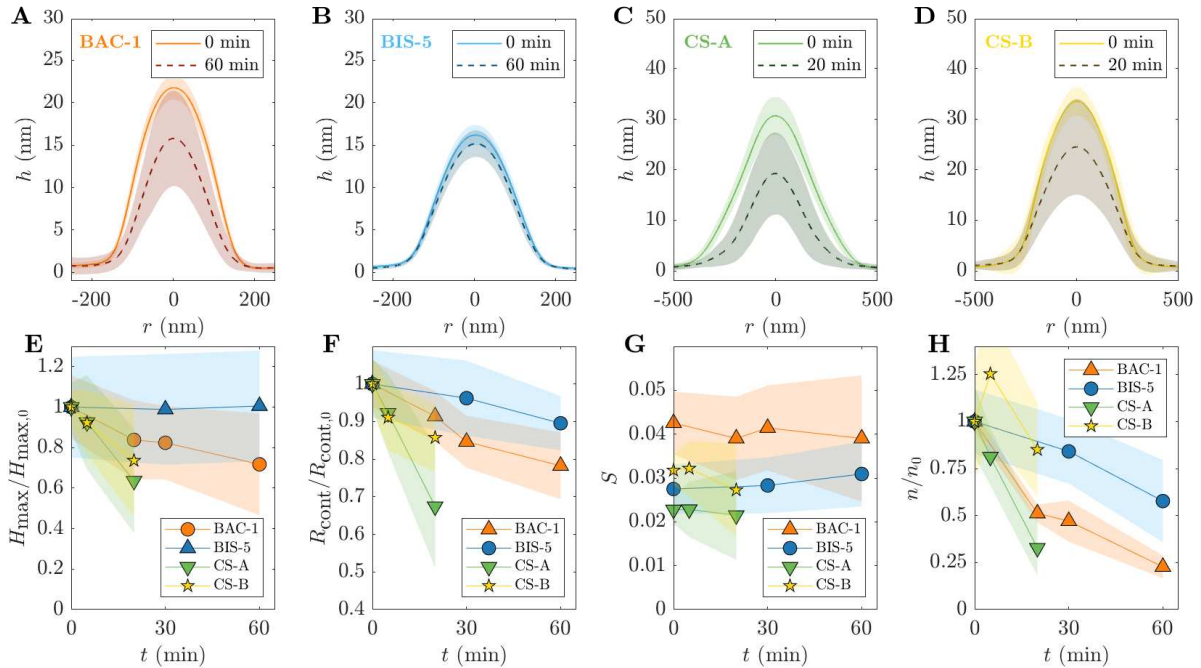


Figure 5: (A-D) Averaged height profiles of BAC-1 microgels, BIS-5 microgels, CS-A microgels and CS-B microgels (left to right) before and after extensive ultrasonication (t indicated in the legend). (E) Mean maximum height of the microgels, H_{\max} , normalized by the pristine value, $H_{\max,0}$, vs. ultrasonication time t . (F) Mean contact radius of the microgels, R_{cont} , normalized by the pristine value, $R_{\text{cont},0}$, vs. t . (G) Mean shape parameter of the adsorbed microgels, $S = H_{\max}/2R_{\text{cont}}$, vs. t . (H) Normalized number densities of the microgels in suspension, n/n_0 , vs. t . Shaded areas in all panels correspond to standard deviation.

Now, we perform a detailed quantitative analysis of the AFM data. Figures 5A-5D compare averaged height profiles of the microgels before (solid lines) and after extensive

ultrasonication (dashed lines) for 60 or 20 min (see legend): BAC-1 (A), BIS-5 (B), CS-A (C) and CS-B (D). The maximum height of the profile decreases for the weaker BAC-1 microgels, Figure 5A, and remains almost the same for the stronger BIS-5 microgels, Figure 5. At the same time, the standard deviation of both height profiles increases (shaded areas), indicating the increase of apparent polydispersity and appearance of ruptured microgels. The shape of the profile remains the same (roughly Gaussian) irrespective of t . The core-shell microgels show the same effects but to a larger extent because of their higher susceptibility to mechanical degradation, Figures 5C, 5D. In agreement with the DLS results, CS-A microgels (panel C) show a larger relative decrease in size compared to the CS-B microgels (panel D). The shape of the profiles, which in this case is different between CS-A and CS-B samples and reflects the different internal structures, remains the same irrespective of t .

Figure 5E shows the mean maximum heights of the microgels H_{\max} (normalized by the value at 0 min, $H_{\max,0}$) *vs.* t . Shaded areas correspond to the standard deviation within the sample. For BAC-1 microgels (orange circles), the decrease of H_{\max} is statistically significant (one-way ANOVA, $p < 0.0001$, Figure S10A) and is the strongest within the first 20 min of ultrasonication. Then, the value decreases slower and reaches $H_{\max} \approx 0.72H_{\max,0}$ after 60 min of ultrasonication. This corresponds to the removal of the periphery of the microgels, including the dangling chains, as also seen from the values of R_h and R_g . On the other hand, the increase of the standard deviation of H_{\max} is likely due to the increasing number of ruptured microgels, which grows significantly at $t = 60$ min. For the BIS-5 microgels (blue upward triangles), no significant change of H_{\max} is observed (one-way ANOVA, $p = 0.852$, Figure S10B). Because the standard deviation of H_{\max} is already quite high for this sample, the appearance of a few ruptured particles (Figure S9) cannot be seen from the averaged height data. The core-shell microgels show a steady decrease of H_{\max} at all investigated ultrasonication times, $t \leq 20$ min (green downward triangles and yellow stars), which is statistically significant (one-way ANOVA, $p < 0.0001$, Figures S11A and S11D). The decrease is slightly larger compared to BAC-1 microgels. In this case, it probably results from the

combination of the removal of the dangling chains and rupture of microgels, *i.e.* the two contributions cannot be separated in time.

Figure 5F shows the mean radii of microgel corona (see Figure 4A, inset): contact radii R_{cont} *vs.* t . The R_{cont} values are also normalized by the value at 0 min, $R_{\text{cont},0}$. All microgels show a significant decrease of $R_{\text{cont}}/R_{\text{cont},0}$ with t (one-way ANOVA, $p < 0.0001$, Figures S10B, S10E, S11B and S11E). The rate of the decrease depends on the susceptibility of a microgel to mechanical degradation: the weaker the microgel the faster is the decrease (BIS-5 < BAC-1 < CS-B < CS-A). Since R_{cont} is mostly sensitive to the dangling chains and peripheral parts of the network, this parameter can be a sensitive measure of their removal, complementary to the ρ -parameter from DLS/SLS (Figure 2C).

Now, the interpretation of the changes in H_{max} and R_{cont} is not straightforward, because the degradation of microgels can influence their capacity to flatten at interfaces where the AFM measurements are performed.⁴⁵ Therefore, the changes in H_{max} and R_{cont} could relate to the altered size, internal structure or flattening capacity (softness) of the degraded microgels. To quantify this capacity, we propose a shape parameter S defined as a quotient of the maximum height H_{max} and the lateral diameter $2R_{\text{cont}}$ of a microgel:

$$S = \frac{H_{\text{max}}}{2R_{\text{cont}}}. \quad (3)$$

The lower the S -parameter, the more a microgel flattens at the interface, *i.e.* the softer it is. Figure 5G shows the mean values of S *vs.* t for the investigated microgels. In all cases except CS-A microgels, the influence of t on the mean value of S is statistically significant despite the large standard deviations (one-way ANOVA, $p < 0.0001$, Figures S10C, S10F, S11C and S11F). However, the trends are different for the different microgels. BIS-5 microgels (blue circles) show a gradual increase of S over the whole investigated t interval, whereby the standard deviation of S (shaded area) increases only slightly. In contrast, BAC-1 microgels (orange upward triangles) show first a small decrease of S at $t = 20$ min, followed by an

equally small increase at $t = 30$ min. At the same time, the standard deviation of S grows significantly with increasing t . CS-B microgels (yellow stars) show a slight decrease of the mean values of S and an increase of its standard deviation similar to BAC-1 microgels. Finally, CS-A microgels (green down triangles) only show an increase of the standard deviation of S with t . To rationalize these non-trivial trends, we note that the removal of the dangling chains and the rupture of microgels are expected to lead to opposite effects on S (increase or decrease, respectively). Therefore, the contribution of each of the two mechanisms at each t needs to be estimated.

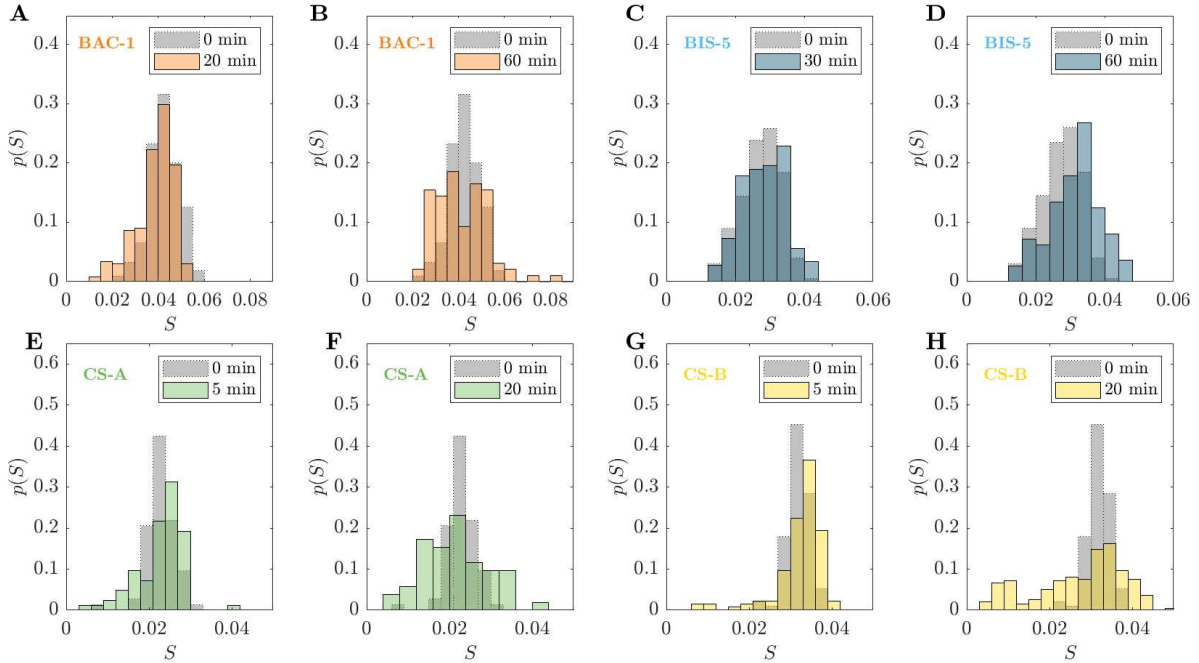


Figure 6: Probability density functions, $p(S)$, of the shape parameter S for BAC-1 microgels (**A,B**), BIS-5 microgels (**C,D**), CS-A microgels (**E,F**) and CS-B microgels (**G,H**) at different ultrasonication times (indicated in the panels).

To achieve this goal, we make use of the particle-tracking algorithms for the analysis of the AFM data (see Experimental section) to calculate the S -parameter for each particle individually. This allows us to obtain the approximate probability density functions (PDFs) of the S -parameter, $p(S)$, after different ultrasonication times and detect the changes in the shape of the S -parameter distribution. Figure 6 shows the $p(S)$ for different microgels at an

early degradation stage (panels A, C, E, G) and a late degradation stage (panels B, D, F, H). The exact ultrasonication times depend on each microgel’s susceptibility to degradation and are indicated in the legend of each panel. The corresponding PDFs of pristine microgels (0 min) are shown as gray bars with a dotted frame.

For BAC-1 microgels at $t = 20$ min, Figure 6A, a small shoulder at $S \approx 0.02 - 0.03$ is observed with respect to the $t = 0$ min, whereas the maximum of the distribution is not affected. After extensive degradation for $t = 60$ min, Figure 6B, this shoulder develops into the second peak at $S \approx 0.03$ resulting in an apparently bimodal distribution of S . At the same time, the first peak shifts to higher $S \approx 0.05$. For BIS-5 microgels at the early degradation stage ($t = 30$ min), Figure 6C, no significant change in the shape of $p(S)$ can be seen. After $t = 60$ min, Figure 6D, the maximum of the distribution shifts to higher S and an indication of a shoulder at $S \approx 0.02$ appears. CS-A microgels develop a broad bimodal distribution of S already after 5 min of ultrasonication, Figure 6E. The main peak shifts to higher S -values whereas the second peak appears at $S \approx 0.018$. After 20 min ultrasonication, the main peak broadens by developing a shoulder at $S \approx 0.03$, while the peak at $S \approx 0.018$ becomes more pronounced, Figure 6F. For CS-B microgels a similar picture is observed: after 5 min the maximum shifts to higher S and a broad shoulder starts to develop at $S \approx 0.02$ with an additional small peak at $S \approx 0.009$. After 20 min, the main peak broadens and decreases in intensity, while the shoulder at $S \approx 0.02$ and a peak at $S \approx 0.009$ grow.

These changes of the PDFs can be assigned to the changes in microgel structure and the extent of its degradation. The gradual shift of the distribution maximum to higher values of S corresponds to the removal of the dangling chains and outermost parts of the microgel network. The resulting microgels are effectively harder and can flatten less at the interface, hence the higher values of S without a strong broadening of the distribution. This effect is seen in all microgels and it is the least affected by the type and amount of crosslinker (susceptibility to degradation). Conversely, the rupture of microgels corresponds to the formation of a shoulder in $p(S)$ at low values of S , which can further develop into the second

maximum. The ruptured microgels are weaker and more affected by the surface forces: adsorption can break them further resulting in very flattened and heterogeneous objects, characterized by low S -values with a broad distribution. The rupture is more pronounced and happens at lower t for microgels that are more susceptible to mechanical degradation, in agreement with our qualitative conclusions from the AFM images.

Finally, we observe that with increasing t larger sample volumes had to be deposited on a substrate to obtain a sufficient number of microgels in the AFM images and have sufficient statistics. In other words, the number concentration of microgels in the samples decreases with t . Since free polymer chains and fragments are removed by this step and the remaining microgels are re-dispersed in the same amount of water, the exact concentration of our samples is unknown. However, it can be estimated by simply counting the microgels in the AFM images. We calculate the number of microgels per unit volume of suspension (number density) n in the samples before and after centrifugation as follows:

$$n = \frac{\langle N \rangle A_{\text{tot}}}{V A_{\text{im}}}, \quad (4)$$

where $\langle N \rangle$ is the average number of microgels per AFM image, A_{tot} is the total area of the interface during deposition (area of the trough), A_{im} is the area of a single AFM image and V is the sample volume deposited on the interface of the trough.

Figure 5H shows the relative number densities n/n_0 for the different microgels *vs.* t . For all microgels, even the most stable BIS-5, n/n_0 decreases significantly as a result of ultrasonication. This means that some microgels are destroyed completely and their fragments are removed by centrifugation. Such a “catastrophic” degradation scenario reveals that the distribution of mechanical forces (or strain rates) experienced by individual microgel particles is very broad. The rate of the n/n_0 decrease correlates with the susceptibility to degradation: it is faster for BAC-1 compared to BIS-5 microgels, $\approx 77\%$ and $\approx 42\%$ of the particles are destroyed after 60 min, respectively. This mass loss is significantly higher than from the

decrease of the mean size (or molecular weight) of the microgels, which is only $\approx 38\%$ for BAC-1 and $\approx 16\%$ for BIS-5 microgels after 60 min (see Figure 1C). The “catastrophic” degradation scenario also explains why for BIS-1 microgels no good data could be obtained at $t > 10$ min. Most of the BIS-1 microgels, which are the weakest microgels studied here, are completely destroyed after > 10 min of ultrasonication.

While the CS-A microgels behave as expected, the CS-B microgels show a non-trivial trend of n/n_0 with increasing t . They first increase the apparent number density at $t = 5$ min and then decrease it at $t = 20$ min. The reason for this can be clearly seen in the AFM images, Figure 4H: many microgel fragments can be seen in the images that are also included in the analysis. So when a core-shell microgel ruptures into several large fragments, the apparent number density n initially increases. As the ultrasonication progresses ($t = 20$ min), the large fragments are also destroyed leading to a decrease in the apparent value of n , as expected. The fact that such a trend is not observed in CS-A microgels could be related to the different rupturing scenario when the core or shell of a core-shell microgel is weaker. Indeed, the fragments seen in the AFM images of CS-A microgels after ultrasonication (Figure 4F) are fewer and smaller compared to the fragments of CS-B microgels after a similar t (Figure 4H). As already mentioned before, the fragments of the conventional microgels (BAC-1 and BIS-5) are much smaller and therefore are removed from the suspension by centrifugation.

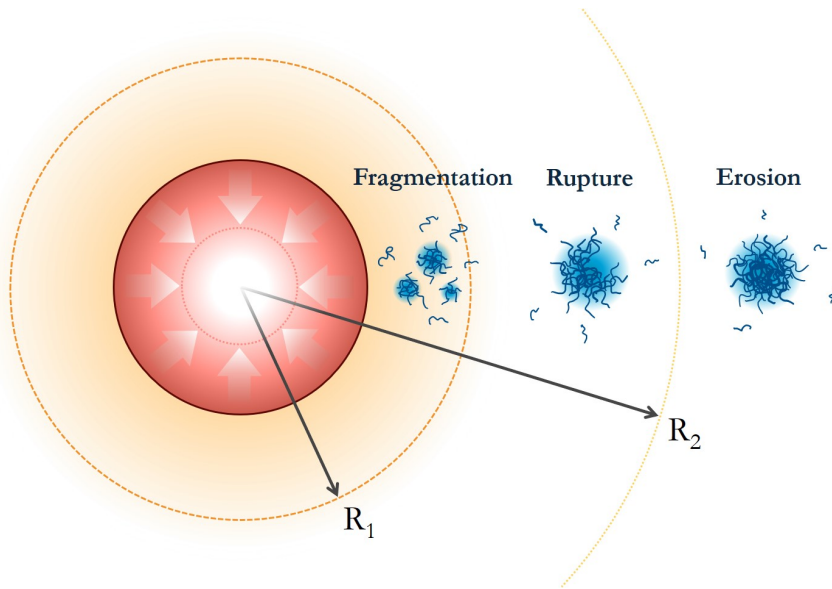
Discussion

Our experimental data shows that the degradation of microgels by ultrasound is a complex process. Unlike linear polymer chains, the susceptibility of a microgel to a mechanical force depends not only on the strength of chemical bonds but also on the network softness, which is closely related to its swelling degree. Using mechanically-labile crosslinks (like disulfides or diselenides) can indeed make the microgels more susceptible to degradation. At the same time, these crosslinks can change the network structure and topology, for example

the distribution of chain lengths or the number of chain entanglements,⁸² or they can make the polymer more hydrophobic. A detailed understanding of the network structure is thus needed to predict and rationally implement mechanical responsiveness in microgels. Here, the future work can build upon the recent progress in designing tough and durable bulk hydrogels⁸³ or elastomers⁸⁴ to implement a desired mechanical responsiveness to the network. Furthermore, many new insights can be gained by comparison of mechanical degradation of microgels with their well-studied chemical degradation.^{62,63,85,86} In particular, the evolution of size and internal structure, as well molecular weight distribution of fragments could be compared.

Our findings that (i) microgels remain fuzzy particles, *i.e.* have a gradually decaying segment density from the center to the periphery, even after extensive degradation and (ii) that selective degradation of the weaker shell or core is not observed in the core-shell microgels suggest that degradation does not happen on the length scale of individual polymer chains. Each discrete degradation step, which is related to a single cavitation event, typically involves the breaking of multiple chemical bonds. In other words, a microgel likely responds to mechanical force as a single elastic body that can deform and break under load. Therefore, understanding how the stress and strain are distributed across the polymer network in a colloidal (mesoscopic) particle is of paramount importance. Here, monomer-resolved computer simulations can give unique insights into the fracture mechanism, as for example in the study by Palkar *et al.* on chemical degradation of nanogels⁸⁶ or in the studies of bulk hydrogel fracture.^{87,88} Experimentally, a reasonable next step could be to analyze the molecular weight distribution of microgel fragments using, for example, analytical ultracentrifugation⁸⁹ or fluid flow fractionation methods.⁶³ Designing a microgel with a selectively degradable shell will likely demand that a large difference in the mechanical strength of the core and shell is achieved. Such that for the average applied force the shell easily breaks but the core is hardly affected.

Finally, the large heterogeneity in the degradation of microgels by ultrasound is one of the



Scheme 2: Schematic illustration of the heterogeneous degradation of microgels in low-concentrated dispersion during inertial cavitation. The collapsing cavitation bubble is shown in red. The R_1 and R_2 are effective cutoff distances for fragmentation and rupture of microgels to occur, respectively.

most interesting findings of this study. The damage experienced by an individual particle over the same ultrasonication time ranges from cleavage of a few dangling chains at the periphery to complete destruction of the particle into fragments. A similar heterogeneity has been observed and intensely investigated in the context of permeabilization and lysis of cells by acoustic cavitation.^{90,91} To explain our results, we propose a qualitative framework similar to the one used by Sundaram *et al.* and Guzmán *et al.* in the cell experiments. First, we consider that the main phenomena responsible for exerting mechanical forces are the wall motion during the expansion-collapse cycle of the cavitation bubble and the shock waves emitted after its collapse. The impact of both effects decay with increasing distance from the bubble center r : the pressure amplitude of the shock wave decreases as $1/r$, while the strain due to the bubble wall motion decreases as $1/r^3$.⁹⁰ Now, for a single cavitation event, we can imagine two (qualitative) cutoff distances from the center of the bubble, R_1 and R_2 , Scheme 2, such that: (i) a microgel located at $r < R_1$ is completely destroyed into fragments, (ii) a microgel located at $R_1 < r < R_2$ is ruptured or forms a crack in its polymer network

and (iii) a microgel located at $r > R_2$ can only undergo a slow erosion by losing its dangling chains. The parameters R_1 and R_2 are expected to depend on the nature of microgels: the weaker the microgels, the higher R_1 and R_2 values should be for a given ultrasound intensity and concentration of air bubbles. The kinetic model for this approach proposed by Sundaram *et al.* predicts the number of particles to decrease exponentially with t , which is approximately what we observe in Figure 5H. The deviations from the exponential course are likely due to inclusion of microgel fragments in the analysis and a large experimental error.

The “erosion” mechanism is most likely responsible for the removal of the dangling chains and microgel periphery, observed by DLS, SLS, AFM (R_{cont}) and discussed in several previous studies.^{54,55,57} This mechanism affects the majority of microgels because it requires the scission of only one covalent bond at a time. However, the “erosion” mechanism also accounts for only a moderate mass loss, see Figure 1C.

The “rupture” mechanism is manifested in the results of form factor analysis by the decrease of R and increase of p , as well as in the AFM images by the irregularly-shaped particles and in the $p(S)$ distributions as the second maximum at low S . This mechanism requires the scission of multiple bonds at once. Therefore, it is less likely to occur than erosion and affects fewer microgels. It is also possible that single broken bonds accumulate in a microgel over the course of ultrasonication and, after some time, result in a rupture event. This scenario would explain why ruptured particles in AFM images and significant changes to the microgel form factors are seen only during the latter stages of degradation.

Lastly, the “fragmentation” mechanism is responsible for the decrease of number concentration of microgels, n , and accounts for the largest polymer mass loss among the three mechanisms. Measurements of n are therefore required in the future studies, for example, using the method proposed by Hildebrandt *et al.*⁹² This mechanism requires the most bond scissions at a time and should therefore be very rare, *e.g.* only in the immediate vicinity of a collapsing cavitation bubble. However, it is possible that fragmentation also occurs *via*

several consecutive rupture events, which might increase its probability. In order to verify if this is indeed the case, a detailed study of the molecular weight distribution is required for both degraded microgels and their fragments.

The above classification offers a simplified picture based on our interpretation of the AFM and scattering data obtained after different sonication times for microgels purified using ultracentrifugation. For a more comprehensive understanding, the small fragments removed by the ultracentrifugation step should be carefully analyzed and included in the discussion. However, we believe that the proposed picture provides a useful framework to explain different degradation scenarios and design new experiments on mechanically-responsive colloids. Further studies could, for example, develop classification algorithms to extract the fractions of intact and degraded microgels from AFM data. Alternatively, one could think of using synthetic microbubbles under stable cavitation conditions to achieve a more homogeneous and controllable strain field.⁹¹ The mechanical force exerted due to bubble wall motion and microstreaming¹⁰ under such conditions might be sufficient to break the weakest bonds: strain rates of $\approx 10^3$ s⁻¹ have been reported at a bubble oscillation amplitude as low as 5% of the bubble radius.⁹³

Conclusion

In this study, we use a combination of several scattering techniques and atomic force microscopy to systematically investigate the mechanism of microgel degradation by high-intensity ultrasound and the role of mechanoresponsive disulfide crosslinks in this process. We show that the susceptibility of a microgel to mechanical degradation results from an interplay between the presence of mechanoresponsive bonds and the swelling degree of the polymer network. Furthermore, we find that the core-shell microgels with different crosslinks in the core and shell cannot be degraded selectively in their weaker part. Instead, the core-shell structure is affected as a whole, and its susceptibility to degradation is close to that of

its weaker part. The mechanism of degradation reflects the large heterogeneity of mechanical forces imposed by the cavitation bubbles on the microgels. The majority of microgels are located far away from the cavitation bubbles and, therefore, experience a relatively weak force. This force leads to a slow erosion of their periphery – dangling chains or weakly crosslinked shell – which can be detected using both light scattering and AFM. In contrast, a small fraction of microgels that are close to a cavitation bubble experience a much stronger force, leading to their rupture or complete disintegration into small fragments. Partial rupture results in microgels with a smaller size and a higher apparent size polydispersity, as seen by the form factor analysis. Furthermore, the ruptured microgels deform stronger upon adsorption at (solid) interfaces than pristine microgels and assume asymmetrical shapes, easily detectable by AFM image analysis. Disintegration of microgels into small fragments is responsible for a significantly higher mass loss compared to both the erosion of the microgel periphery and the partial rupture of their polymer network. This mechanism remains largely unexplored in the literature because a measurement of particle number concentration is needed to confirm it. Overall, our findings highlight the high complexity in mechanical degradation of polymeric microgels, which bears similarities with both the degradation of linear polymers and failure of bulk hydrogels. Our observations can inspire further studies of the extreme mechanics of mesoscopic polymer particles like microgels. Such studies will provide a solid background for the rational design of ultrasound-responsive drug delivery systems and help to address the problems related to formation and spreading of microplastics.

Author Contribution Statement

Alexander V. Petrunin: conceptualization, investigation (DLS, SLS, SAXS, AFM, ultracentrifugation), formal analysis, data curation, writing - original draft; Susanne Braun: conceptualization, investigation (synthesis, DLS, reaction calorimetry, Raman spectroscopy,

ultrasonication), formal analysis, writing - original draft; Felix J. Byn: investigation (DLS, SLS, AFM), formal analysis; Indré Milvydaité: investigation (synthesis); Timon Kratzenberg: software (AFM analysis script); Pablo Mota-Santiago: investigation (SAXS); Andrea Scotti: investigation (SAXS), supervision, writing - review & editing; Andrij Pich: conceptualization, funding acquisition, project administration, supervision, writing - review & editing; Walter Richtering: conceptualization, funding acquisition, project administration, supervision, writing - review & editing.

Data Availability Statement

All data used in the manuscript are available from the authors upon reasonable request.

Acknowledgement

The authors thank the Deutsche Forschungsgemeinschaft for financial support within the SFB 985 “Functional microgels and microgel systems”. Andrea Scotti acknowledges financial support from the Knut and Alice Wallenberg Foundation (Wallenberg Academy Fellows) and from the Swedish Research Council (Research Grant 2024-04178). The SAXS measurements were performed on the CoSAXS beamline at the MAX IV laboratory (Lund, Sweden) under the proposal 20220526. The Research conducted at MAX IV, a Swedish national user facility, is supported by the Swedish Research council under contract 2018-07152, the Swedish Governmental Agency for Innovation Systems under contract 2018-04969, and Formas under contract 2019-02496.

Supporting Information Available

Amounts of chemicals used for the synthesis of microgels; Raman spectroscopy data and the calibration curve; In-line reaction calorimetry data; Discussion of the difference in swelling

degree between BIS- and BAC-crosslinked microgels; Additional DLS, SLS, SAXS data and fit parameters; Additional AFM data.

References

1. Mason, T. J. Therapeutic ultrasound an overview. *Ultrasonics sonochemistry* **2011**, *18*, 847–852.
2. Barnett, S. B.; Rott, H.-D.; ter Haar, G. R.; Ziskin, M. C.; Maeda, K. The sensitivity of biological tissue to ultrasound. *Ultrasound in medicine & biology* **1997**, *23*, 805–812.
3. Pitt, W. G.; Husseini, G. A.; Staples, B. J. Ultrasonic drug delivery—a general review. *Expert opinion on drug delivery* **2004**, *1*, 37–56.
4. Yildiz, D.; Göstl, R.; Herrmann, A. Sonopharmacology: controlling pharmacotherapy and diagnosis by ultrasound-induced polymer mechanochemistry. *Chemical Science* **2022**, *13*, 13708–13719.
5. Suslick, K. S. Sonochemistry. *science* **1990**, *247*, 1439–1445.
6. Ghanem, M. A.; Basu, A.; Behrou, R.; Boechler, N.; Boydston, A. J.; Craig, S. L.; Lin, Y.; Lynde, B. E.; Nelson, A.; Shen, H.; others The role of polymer mechanochemistry in responsive materials and additive manufacturing. *Nature Reviews Materials* **2021**, *6*, 84–98.
7. Lauterborn, W.; Hentschel, W. Cavitation bubble dynamics studied by high speed photography and holography: part one. *Ultrasonics* **1985**, *23*, 260–268.
8. Akhatov, I.; Lindau, O.; Topolnikov, A.; Mettin, R.; Vakhitova, N.; Lauterborn, W. Collapse and rebound of a laser-induced cavitation bubble. *Physics of Fluids* **2001**, *13*, 2805–2819.
9. Lauterborn, W.; Kurz, T. Physics of bubble oscillations. *Reports on progress in physics* **2010**, *73*, 106501.
10. Nyborg, W. Ultrasonic microstreaming and related phenomena. *The British journal of cancer. Supplement* **1982**, *5*, 156.

11. Caruso, M. M.; Davis, D. A.; Shen, Q.; Odom, S. A.; Sottos, N. R.; White, S. R.; Moore, J. S. Mechanically-induced chemical changes in polymeric materials. *Chemical reviews* **2009**, *109*, 5755–5798.
12. Pecha, R.; Gompf, B. Microimplosions: cavitation collapse and shock wave emission on a nanosecond time scale. *Physical review letters* **2000**, *84*, 1328.
13. Glynn, P.; Van Der Hoff, B.; Reilly, P. A general model for prediction of molecular weight distributions of degraded polymers. Development and comparison with ultrasonic degradation experiments. *Journal of Macromolecular Science—Chemistry* **1972**, *6*, 1653–1664.
14. Basedow, A. M.; Ebert, K. H. *Advances in Polymer Science*; Springer, 1977; pp 83–148.
15. Berkowski, K. L.; Potisek, S. L.; Hickenboth, C. R.; Moore, J. S. Ultrasound-induced site-specific cleavage of azo-functionalized poly (ethylene glycol). *Macromolecules* **2005**, *38*, 8975–8978.
16. Göstl, R.; Sijbesma, R. π -extended anthracenes as sensitive probes for mechanical stress. *Chemical science* **2016**, *7*, 370–375.
17. Zhang, H.; Li, X.; Lin, Y.; Gao, F.; Tang, Z.; Su, P.; Zhang, W.; Xu, Y.; Weng, W.; Boulatov, R. Multi-modal mechanophores based on cinnamate dimers. *Nature communications* **2017**, *8*, 1147.
18. Chen, Z.; Zhu, X.; Yang, J.; Mercer, J. A.; Burns, N. Z.; Martinez, T. J.; Xia, Y. The cascade unzipping of ladderane reveals dynamic effects in mechanochemistry. *Nature Chemistry* **2020**, *12*, 302–309.
19. Muramatsu, T.; Okado, Y.; Traeger, H.; Schrettl, S.; Tamaoki, N.; Weder, C.; Sagara, Y. Rotaxane-based dual function mechanophores exhibiting reversible and irreversible responses. *Journal of the American Chemical Society* **2021**, *143*, 9884–9892.

20. Shi, Z.; Wu, J.; Song, Q.; Gööstl, R.; Herrmann, A. Toward drug release using polymer mechanochemical disulfide scission. *Journal of the American Chemical Society* **2020**, *142*, 14725–14732.

21. Huo, S.; Zhao, P.; Shi, Z.; Zou, M.; Yang, X.; Warszawik, E.; Loznik, M.; Gööstl, R.; Herrmann, A. Mechanochemical bond scission for the activation of drugs. *Nature chemistry* **2021**, *13*, 131–139.

22. Zou, M.; Zhao, P.; Fan, J.; Gööstl, R.; Herrmann, A. Microgels as drug carriers for sonopharmacology. *Journal of Polymer Science* **2022**, *60*, 1864–1870.

23. Zhang, H.; Lin, Y.; Xu, Y.; Weng, W. Mechanochemistry of topological complex polymer systems. *Polymer Mechanochemistry* **2015**, 135–207.

24. Chen, J.; Ratnayaka, S.; Alford, A.; Kozlovskaya, V.; Liu, F.; Xue, B.; Hoyt, K.; Kharlampieva, E. Theranostic multilayer capsules for ultrasound imaging and guided drug delivery. *ACS nano* **2017**, *11*, 3135–3146.

25. Wu, P.; Jia, Y.; Qu, F.; Sun, Y.; Wang, P.; Zhang, K.; Xu, C.; Liu, Q.; Wang, X. Ultrasound-responsive polymeric micelles for sonoporation-assisted site-specific therapeutic action. *ACS applied materials & interfaces* **2017**, *9*, 25706–25716.

26. Rifaie-Graham, O.; Galensowske, N. F.; Dean, C.; Pollard, J.; Balog, S.; Gouveia, M. G.; Chami, M.; Vian, A.; Amstad, E.; Lattuada, M.; others Shear Stress-Responsive Polymeromesome Nanoreactors Inspired by the Marine Bioluminescence of Dinoflagellates. *Angewandte Chemie International Edition* **2021**, *60*, 904–909.

27. Epstein-Barash, H.; Orbey, G.; Polat, B. E.; Ewoldt, R. H.; Feshitan, J.; Langer, R.; Borden, M. A.; Kohane, D. S. A microcomposite hydrogel for repeated on-demand ultrasound-triggered drug delivery. *Biomaterials* **2010**, *31*, 5208–5217.

28. Fang, K.; Wang, R.; Zhang, H.; Zhou, L.; Xu, T.; Xiao, Y.; Zhou, Y.; Gao, G.; Chen, J.; Liu, D.; others Mechano-responsive, tough, and antibacterial zwitterionic hydrogels with controllable drug release for wound healing applications. *ACS Applied Materials & Interfaces* **2020**, *12*, 52307–52318.

29. Di, J.; Yu, J.; Wang, Q.; Yao, S.; Suo, D.; Ye, Y.; Pless, M.; Zhu, Y.; Jing, Y.; Gu, Z. Ultrasound-triggered noninvasive regulation of blood glucose levels using microgels integrated with insulin nanocapsules. *Nano Research* **2017**, *10*, 1393–1402.

30. Karg, M.; Pich, A.; Hellweg, T.; Hoare, T.; Lyon, L. A.; Crassous, J.; Suzuki, D.; Gumerov, R. A.; Schneider, S.; Potemkin, I. I.; others Nanogels and microgels: From model colloids to applications, recent developments, and future trends. *Langmuir* **2019**, *35*, 6231–6255.

31. Scheffold, F. Pathways and challenges towards a complete characterization of microgels. *Nature communications* **2020**, *11*, 4315.

32. Fernández-Barbero, A.; Fernández-Nieves, A.; Grillo, I.; López-Cabarcos, E. Structural modifications in the swelling of inhomogeneous microgels by light and neutron scattering. *Physical Review E* **2002**, *66*, 051803.

33. Fernández-Nieves, A.; Fernández-Barbero, A.; Vincent, B.; De Las Nieves, F. Charge controlled swelling of microgel particles. *Macromolecules* **2000**, *33*, 2114–2118.

34. Fernández-Nieves, A.; Fernández-Barbero, A.; De las Nieves, F. Salt effects over the swelling of ionized mesoscopic gels. *The Journal of Chemical Physics* **2001**, *115*, 7644–7649.

35. Lopez, C. G.; Richtering, W. Does Flory–Rehner theory quantitatively describe the swelling of thermoresponsive microgels? *Soft Matter* **2017**, *13*, 8271–8280.

36. Braun, S.; Santi, M.; Demco, D. E.; Litzen, I.; Uecker, J.; Fechete, R.; Walkowiak, J. J.; Pich, A. Investigation of morphology and volume phase transition of supramacromolecular microgels by NMR spectroscopy and quartz crystal microbalance. *Journal of Polymer Science* **2024**, *62*, 2301–2319.

37. Nolan, C. M.; Gelbaum, L. T.; Lyon, L. A. H NMR investigation of thermally triggered insulin release from poly (N-isopropylacrylamide) microgels. *Biomacromolecules* **2006**, *7*, 2918–2922.

38. Braun, S.; Dilarri, G.; de Lencastre Novaes, L. C.; Huth, P.; Töpel, A.; Hussmann, L.; Boes, A.; da Rocha, M. D.; Jakob, F.; Regasini, L. O.; others Hexyl gallate loaded microgels enable efficient protection against citrus canker. *Advanced Functional Materials* **2024**, *34*, 2305646.

39. Gawlitzta, K.; Georgieva, R.; Tavraz, N.; Keller, J.; von Klitzing, R. Immobilization of water-soluble HRP within poly-N-isopropylacrylamide microgel particles for use in organic media. *Langmuir* **2013**, *29*, 16002–16009.

40. Sigolaeva, L. V.; Gladyr, S. Y.; Gelissen, A. P.; Mergel, O.; Pergushov, D. V.; Kurochkin, I. N.; Plamper, F. A.; Richtering, W. Dual-stimuli-sensitive microgels as a tool for stimulated spongelike adsorption of biomaterials for biosensor applications. *Biomacromolecules* **2014**, *15*, 3735–3745.

41. Gawlitzta, K.; Turner, S. T.; Polzer, F.; Wellert, S.; Karg, M.; Mulvaney, P.; von Klitzing, R. Interaction of gold nanoparticles with thermoresponsive microgels: influence of the cross-linker density on optical properties. *Physical Chemistry Chemical Physics* **2013**, *15*, 15623–15631.

42. Brasili, F.; Del Monte, G.; Capocefalo, A.; Chauveau, E.; Buratti, E.; Casciardi, S.; Truzzolillo, D.; Sennato, S.; Zaccarelli, E. Toward a unified description of the electrostatic

assembly of microgels and nanoparticles. *ACS Applied Materials & Interfaces* **2023**, *15*, 58770–58783.

43. Voudouris, P.; Florea, D.; van der Schoot, P.; Wyss, H. M. Micromechanics of temperature sensitive microgels: dip in the Poisson ratio near the LCST. *Soft Matter* **2013**, *9*, 7158–7166.

44. Schulte, M. F.; Bochenek, S.; Brugnoni, M.; Scotti, A.; Mourran, A.; Richtering, W. Stiffness tomography of ultra-soft nanogels by atomic force microscopy. *Angewandte Chemie International Edition* **2021**, *60*, 2280–2287.

45. Scotti, A.; Schulte, M. F.; Lopez, C. G.; Crassous, J. J.; Bochenek, S.; Richtering, W. How softness matters in soft nanogels and nanogel assemblies. *Chemical reviews* **2022**, *122*, 11675–11700.

46. Schulte, M. F.; Izak-Nau, E.; Braun, S.; Pich, A.; Richtering, W.; Göstl, R. Microgels react to force: mechanical properties, syntheses, and force-activated functions. *Chemical Society Reviews* **2022**, *51*, 2939–2956.

47. Stock, S.; von Klitzing, R.; Rahimzadeh, A. Dynamic light scattering for particle characterization subjected to ultrasound: a study on compact particles and acousto-responsive microgels. *Scientific Reports* **2024**, *14*, 989.

48. Rahimzadeh, A.; Rutsch, M.; Kupnik, M.; Klitzing, R. v. Visualization of acoustic energy absorption in confined aqueous solutions by PNIPAM microgels: Effects of bulk viscosity. *Langmuir* **2021**, *37*, 5854–5863.

49. Venegas-Sanchez, J. A.; Kusunoki, T.; Yamamoto, M.; Kobayashi, T. Sono-respond on thermosensitive polymer microgels based on cross-linked poly (N-isopropylacrylamide-co-acrylic acid). *Ultrasonics sonochemistry* **2013**, *20*, 1271–1275.

50. Joshi, A.; Nandi, S.; Chester, D.; Brown, A. C.; Muller, M. Study of poly (N-isopropylacrylamide-co-acrylic acid)(pNIPAM) microgel particle induced deformations of tissue-mimicking phantom by ultrasound stimulation. *Langmuir* **2018**, *34*, 1457–1465.

51. Vukićević, R.; Neffe, A. T.; Luetzow, K.; Pierce, B. F.; Lendlein, A. Conditional Ultrasound Sensitivity of Poly [(N-isopropylacrylamide)-co-(vinyl imidazole)] Microgels for Controlled Lipase Release. *Macromolecular rapid communications* **2015**, *36*, 1891–1896.

52. Lei, B.; Chen, M.; Wang, Y.; Zhang, J.; Xu, S.; Liu, H. Double security drug delivery system DDS constructed by multi-responsive (pH/redox/US) microgel. *Colloids and Surfaces B: Biointerfaces* **2020**, *193*, 111022.

53. Kubota, T.; Kurashina, Y.; Zhao, J.; Ando, K.; Onoe, H. Ultrasound-triggered on-demand drug delivery using hydrogel microbeads with release enhancer. *Materials & Design* **2021**, *203*, 109580.

54. Kharandiuk, T.; Tan, K. H.; Xu, W.; Weitenhagen, F.; Braun, S.; Göstl, R.; Pich, A. Mechanoresponsive diselenide-crosslinked microgels with programmed ultrasound-triggered degradation and radical scavenging ability for protein protection. *Chemical Science* **2022**, *13*, 11304–11311.

55. He, S.; Schog, S.; Chen, Y.; Ji, Y.; Panitz, S.; Richtering, W.; Göstl, R. Photoinduced Mechanical Cloaking of Diarylethene-Crosslinked Microgels. *Advanced Materials* **2023**, *35*, 2305845.

56. Izak-Nau, E.; Braun, S.; Pich, A.; Göstl, R. Mechanically Resistant Poly (N-vinylcaprolactam) Microgels with Sacrificial Supramolecular Catechin Hydrogen Bonds. *Advanced Science* **2022**, *9*, 2104004.

57. Izak-Nau, E.; Demco, D. E.; Braun, S.; Baumann, C.; Pich, A.; Göstl, R. Shear-induced structural and functional transformations of poly (N-vinylcaprolactam) microgels. *ACS Applied Polymer Materials* **2020**, *2*, 1682–1691.

58. Schulte, M. F.; Scotti, A.; Gelissen, A. P.; Richtering, W.; Mourran, A. Probing the internal heterogeneity of responsive microgels adsorbed to an interface by a sharp SFM tip: Comparing core–shell and hollow microgels. *Langmuir* **2018**, *34*, 4150–4158.

59. Bochenek, S.; Scotti, A.; Ogieglo, W.; Fernández-Rodríguez, M. A.; Schulte, M. F.; Gumerov, R. A.; Bushuev, N. V.; Potemkin, I. I.; Wessling, M.; Isa, L.; others Effect of the 3D swelling of microgels on their 2D phase behavior at the liquid–liquid interface. *Langmuir* **2019**, *35*, 16780–16792.

60. Schulte, M. F.; Scotti, A.; Brugnoni, M.; Bochenek, S.; Mourran, A.; Richtering, W. Tuning the structure and properties of ultra-low cross-linked temperature-sensitive microgels at interfaces via the adsorption pathway. *Langmuir* **2019**, *35*, 14769–14781.

61. Nishizawa, Y.; Matsui, S.; Urayama, K.; Kureha, T.; Shibayama, M.; Uchihashi, T.; Suzuki, D. Non-Thermoresponsive Decanano-sized Domains in Thermoresponsive Hydrogel Microspheres Revealed by Temperature-Controlled High-Speed Atomic Force Microscopy. *Angewandte Chemie International Edition* **2019**, *58*, 8809–8813.

62. Nishizawa, Y.; Yokoi, H.; Uchihashi, T.; Suzuki, D. Single microgel degradation governed by heterogeneous nanostructures. *Soft matter* **2023**, *19*, 5068–5075.

63. Gaulding, J. C.; Smith, M. H.; Hyatt, J. S.; Fernandez-Nieves, A.; Lyon, L. A. Reversible inter-and intra-microgel cross-linking using disulfides. *Macromolecules* **2012**, *45*, 39–45.

64. Plivelic, T. S.; Terry, A. E.; Appio, R.; Theodor, K.; Klementiev, K. X-ray tracing, design and construction of an optimized optics scheme for CoSAXS, the small angle x-ray scattering beamline at MAX IV laboratory. AIP Conference Proceedings. 2019; p 030013.

65. Stieger, M.; Richtering, W.; Pedersen, J. S.; Lindner, P. Small-angle neutron scattering study of structural changes in temperature sensitive microgel colloids. *The Journal of chemical physics* **2004**, *120*, 6197–6206.

66. Berndt, I.; Pedersen, J. S.; Richtering, W. Structure of multiresponsive “intelligent” core- shell microgels. *Journal of the American Chemical Society* **2005**, *127*, 9372–9373.

67. Dubbert, J.; Honold, T.; Pedersen, J. S.; Radulescu, A.; Drechsler, M.; Karg, M.; Richtering, W. How hollow are thermoresponsive hollow nanogels? *Macromolecules* **2014**, *47*, 8700–8708.

68. Virtanen, O.; Mourran, A.; Pinard, P.; Richtering, W. Persulfate initiated ultra-low cross-linked poly (N-isopropylacrylamide) microgels possess an unusual inverted cross-linking structure. *Soft matter* **2016**, *12*, 3919–3928.

69. Nečas, D.; Klapetek, P. Gwyddion: an open-source software for SPM data analysis. *Open Physics* **2012**, *10*, 181–188.

70. Crocker, J. C.; Grier, D. G. Methods of Digital Video Microscopy for Colloidal Studies. *Journal of Colloid and Interface Science* **1996**, *179*, 298–310.

71. Pelton, R. H.; Chibante, P. Preparation of aqueous latices with N-isopropylacrylamide. *Colloids and surfaces* **1986**, *20*, 247–256.

72. Berndt, I.; Richtering, W. Doubly Temperature Sensitive Core- Shell Microgels. *Macromolecules* **2003**, *36*, 8780–8785.

73. Houston, J. E.; Fruhner, L.; de la Cotte, A.; Rojo González, J.; Petrunin, A. V.; Gasser, U.; Schweins, R.; Allgaier, J.; Richtering, W.; Fernandez-Nieves, A.; others Resolving the different bulk moduli within individual soft nanogels using small-angle neutron scattering. *Science advances* **2022**, *8*, eabn6129.

74. Metze, F. K.; Sant, S.; Meng, Z.; Klok, H.-A.; Kaur, K. Swelling-activated, soft mechanochemistry in polymer materials. *Langmuir* **2023**, *39*, 3546–3557.

75. Glatter, O. *Scattering methods and their application in colloid and interface science*; Elsevier, 2018.

76. Senff, H.; Richtering, W. Influence of cross-link density on rheological properties of temperature-sensitive microgel suspensions. *Colloid and Polymer Science* **2000**, *278*, 830–840.

77. Pich, A.; Tessier, A.; Boyko, V.; Lu, Y.; Adler, H.-J. P. Synthesis and characterization of poly (vinylcaprolactam)-based microgels exhibiting temperature and pH-sensitive properties. *Macromolecules* **2006**, *39*, 7701–7707.

78. Clara-Rahola, J.; Fernandez-Nieves, A.; Sierra-Martin, B.; South, A.; Lyon, L. A.; Kohlbrecher, J.; Fernandez Barbero, A. Structural properties of thermoresponsive poly (N-isopropylacrylamide)-poly (ethyleneglycol) microgels. *The Journal of Chemical Physics* **2012**, *136*.

79. Elancheliyan, R.; Del Monte, G.; Chauveau, E.; Sennato, S.; Zaccarelli, E.; Truzzolillo, D. Role of charge content in the two-step deswelling of Poly (N-isopropylacrylamide)-based microgels. *Macromolecules* **2022**, *55*, 7526–7539.

80. Gasser, U.; Hyatt, J.; Lietor-Santos, J.-J.; Herman, E.; Lyon, L. A.; Fernandez-Nieves, A. Form factor of pNIPAM microgels in overpacked states. *The Journal of chemical physics* **2014**, *141*.

81. Mohanty, P. S.; Nöjd, S.; van Gruijthuijsen, K.; Crassous, J. J.; Obiols-Rabasa, M.; Schweins, R.; Stradner, A.; Schurtenberger, P. Interpenetration of polymeric microgels at ultrahigh densities. *Scientific Reports* **2017**, *7*, 1487.

82. Shen, J.; Lin, X.; Liu, J.; Li, X. Effects of cross-link density and distribution on static and dynamic properties of chemically cross-linked polymers. *Macromolecules* **2018**, *52*, 121–134.

83. Zhao, X.; Chen, X.; Yuk, H.; Lin, S.; Liu, X.; Parada, G. Soft materials by design: unconventional polymer networks give extreme properties. *Chemical Reviews* **2021**, *121*, 4309–4372.

84. Ducrot, E.; Chen, Y.; Bulters, M.; Sijbesma, R. P.; Creton, C. Toughening elastomers with sacrificial bonds and watching them break. *Science* **2014**, *344*, 186–189.

85. Smith, M. H.; Herman, E. S.; Lyon, L. A. Network deconstruction reveals network structure in responsive microgels. *The Journal of Physical Chemistry B* **2011**, *115*, 3761–3764.

86. Palkar, V.; Thakar, D.; Kuksenok, O. Nanogel degradation at soft interfaces and in bulk: tracking shape changes and interfacial spreading. *Macromolecules* **2023**, *56*, 1289–1302.

87. Boots, J.; Brake, D. t.; Clough, J. M.; Tauber, J.; Ruiz-Franco, J.; Kodger, T.; Van Der Gucht, J. Quantifying bond rupture during indentation fracture of soft polymer networks using molecular mechanophores. *Physical Review Materials* **2022**, *6*, 025605.

88. Tauber, J.; Van Der Gucht, J.; Dussi, S. Stretchy and disordered: Toward understanding fracture in soft network materials via mesoscopic computer simulations. *The Journal of Chemical Physics* **2022**, *156*.

89. Tauer, K.; Gau, D.; Schulze, S.; Völkel, A.; Dimova, R. Thermal property changes of poly (N-isopropylacrylamide) microgel particles and block copolymers. *Colloid and Polymer Science* **2009**, *287*, 299–312.

90. Sundaram, J.; Mellein, B. R.; Mitragotri, S. An experimental and theoretical analysis of ultrasound-induced permeabilization of cell membranes. *Biophysical journal* **2003**, *84*, 3087–3101.

91. Guzmán, H. R.; McNamara, A. J.; Nguyen, D. X.; Prausnitz, M. R. Bioeffects caused by changes in acoustic cavitation bubble density and cell concentration: a unified explanation based on cell-to-bubble ratio and blast radius. *Ultrasound in medicine & biology* **2003**, *29*, 1211–1222.

92. Hildebrandt, M.; Lazarev, S.; Pérez, J.; Vartanyants, I. A.; Meijer, J.-M.; Karg, M. SAXS Investigation of Core–Shell Microgels with High Scattering Contrast Cores: Access to Structure Factor and Volume Fraction. *Macromolecules* **2022**, *55*, 2959–2969.

93. Marmottant, P.; Hilgenfeldt, S. Controlled vesicle deformation and lysis by single oscillating bubbles. *Nature* **2003**, *423*, 153–156.

Supporting Information.

Unraveling the Mechanisms of Ultrasound-Induced Mechanical Degradation of Microgels: Effects of Mechanoresponsive Crosslinks, Softness, and Core-Shell Architecture

Alexander V. Petrunin,^{†,‡,∇} Susanne Braun,^{¶,§,∇} Felix J. Byn,[‡] Indré Milvydaité,^{||,§} Timon Kratzenberg,[‡] Pablo Mota-Santiago,^{⊥,♯} Andrea Scotti,[ⓐ] Andrij Pich,^{¶,§,△} and Walter Richtering^{*,‡}

[†]*Institute of Experimental Colloidal Physics, Heinrich-Heine University, Universitätsstr. 1, Düsseldorf, Germany*

[‡]*Institute of Physical Chemistry, RWTH Aachen University, Landoltweg 2, 52074 Aachen, Germany, EU*

[¶]*DWI – Leibniz Institute for Interactive Materials, Forckenbeckstr. 50, 52074 Aachen, Germany, EU*

[§]*Functional and Interactive Polymers, Institute of Technical and Macromolecular Chemistry (ITMC), RWTH Aachen University, Worringerweg 2, 52074 Aachen, Germany, EU*

^{||}*DWI – Leibniz Institute for Interactive Materials e. V., Forckenbeckstr. 50, 52074 Aachen, Germany, EU*

[⊥]*Australian Synchrotron, ANSTO, Clayton, Victoria, Australia*

[#]*MAX IV Laboratory, Lund University, P.O. Box 118, 22100 Lund, Sweden, EU*

[ⓐ]*Division of Physical Chemistry, Lund University, SE-22100 Lund, Sweden*

[△]*Aachen Maastricht Institute for Biobased Materials (AMIBM), Maastricht University, Brightlands Chemelot Campus, Urmonderbaan 22, 6167 RD Geleen, The Netherlands, EU*

[∇]*These authors contributed equally to this work.*

E-mail: richtering@pc.rwth-aachen.de

S1. Amounts of Chemicals and Other Details to the Syntheses of Microgels

Table S1: Internal sample codes (lab journal) of the microgels used in the main manuscript.

Microgel	Sample code in the lab journal
BIS-1	SB-C6
BAC-1	SB-1BAC
BIS-5	SB-5BIS
BAC-5	SB-5BAC
CS-A	IM-12
CS-B	IM-18

Table S2: Exact amounts of chemicals used for the syntheses of the conventional microgels used in the main manuscript.

Name	Crosslinker content	Reaction vessel	$m(\text{NIPAm})$ [g]	$m(\text{BIS})$ [g]	$m(\text{BAC})$ [g]	$m(\text{SDS})$ [g]	$m(\text{TEMED})$ [g]	$m(\text{APS})$ [g]	$V(\text{H}_2\text{O})$ [mL]
BIS-1	1 mol% BIS	flask			-				
BIS-5	5 mol% BIS	calorimeter			-				
BAC-1	1 mol% BAC	calorimeter	4.0000	-	0.0921	0.0417	0.0411	0.0810	300.79
BAC-5	5 mol% BAC	calorimeter	4.0000	-	0.4701	0.0425	0.0411	0.0805	300.08

Table S3: Exact amounts of chemicals used for the syntheses of conventional microgels used as cores for the core-shell microgels.

Name	Crosslinker content	$m(\text{NIPAm})$ [g]	$m(\text{BIS})$ [g]	$m(\text{BAC})$ [g]	$m(\text{SDS})$ [g]	$V(\text{TEMED})$ [μL]	$m(\text{APS})$ [g]	$V(\text{H}_2\text{O})$ [mL]
CS-A core	1 mol% BAC	2.001	-	0.048	0.021	26.5	0.041	150
CS-B core	1 mol% BIS	1.087	0.015	-	0.017	14.1	0.022	80

Table S4: Characteristics of the conventional microgels used as cores for the core-shell microgels.

Name	Crosslinker content	$c(\text{microgel})$ [$\text{mg} \cdot \text{mL}^{-1}$]	yield [%]	$R_h(20^\circ\text{C})$ [nm]	PDI [a.u.]	$R_h(60^\circ\text{C})$ [nm]	PDI [a.u.]
CS-A core	1 mol% BAC	12.7	90.3	124 ± 1.46	0.0136 ± 0.0074	68 ± 0.74	0.0152 ± 0.0106
CS-B core	1 mol% BIS	10.7	75.4	134 ± 2.77	0.0103 ± 0.0080	53 ± 0.42	0.0177 ± 0.0118

Table S5: Exact amounts of chemicals used for the syntheses of the shell of the core-shell microgels.

Name	Crosslinker content	$V(\text{core solution})$ [mL]	$m(\text{NIPAm})$ [g]	$m(\text{BIS})$ [g]	$m(\text{BAC})$ [g]	$V(\text{TEMED})$ [μL]	$m(\text{APS})$ [g]	$V(\text{H}_2\text{O})$ [mL]
CS-A	1 mol% BAC/1 mol% BIS		1.201	0.016	-	15.9	0.024	60
CS-B	1 mol% BIS/1 mol% BAC		1.201	-	0.028	15.9	0.025	60

S2. Determination of BAC Content in the Microgels Using Raman Spectroscopy

In order to quantify how much disulfide bonds remain in the BAC-crosslinked microgels, we performed Raman spectroscopy measurements. The amount of S-S groups was calculated from their characteristic peak at $\approx 500 \text{ cm}^{-1}$, Figure S1, using a calibration curve obtained by mixing known amounts of homopolymers (pNIPAm and pBAC), Figure S2. For the microgels with nominal amounts of BAC crosslinker equal to 1, 3 and 5 mol%, we found the actual BAC contents of 0.3, 1.8 and 3.2 mol%, respectively.

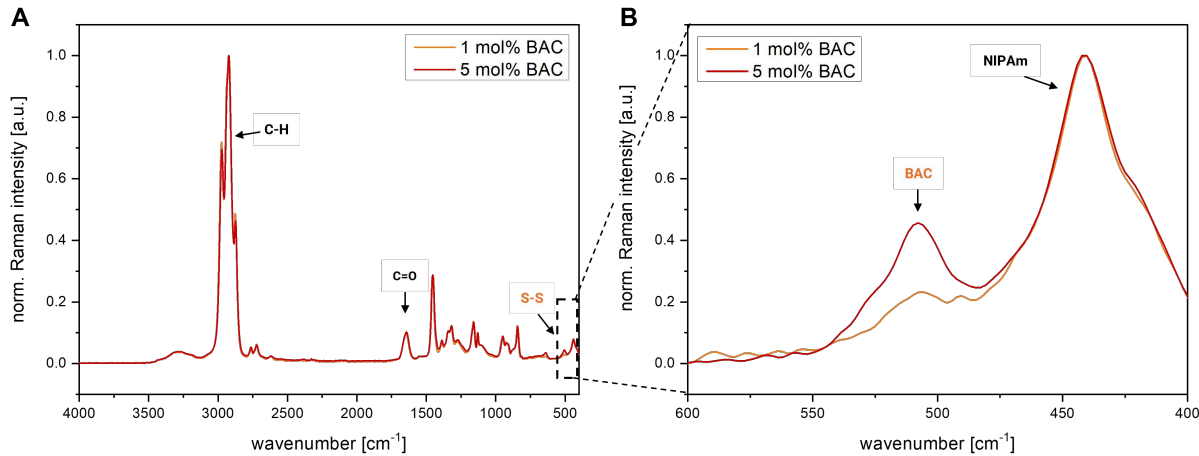


Figure S1: Fourier Transform Raman spectra of BAC-crosslinked pNIPAm microgels with 1 and 5 mol% of theoretical crosslinker content. (A) Total Raman spectrum, and (B) enlarged view on the characteristic disulfide-bond region.

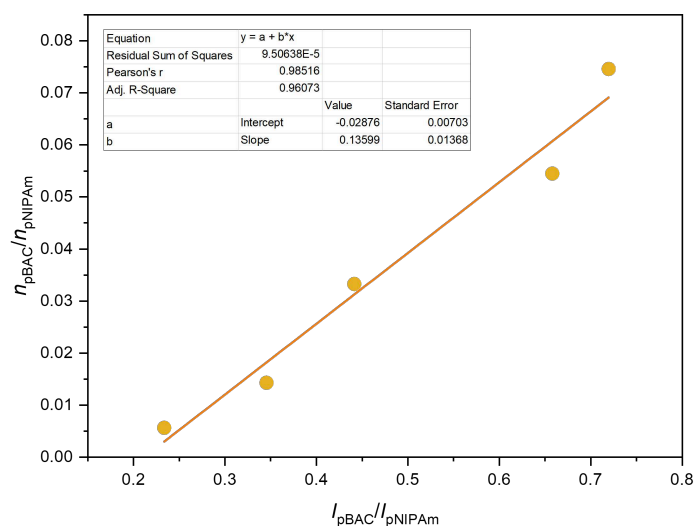


Figure S2: Raman calibration curve used to quantify the BAC content incorporated into the microgel network and obtained by mixing of homopolymers of pNIPAm and pBAC.

S3. Monitoring the Kinetics of the Microgel Syntheses Using In-Line Reaction Calorimetry

To better understand the difference between BIS- and BAC-crosslinked microgels, their polymerization kinetics were followed using in-line reaction calorimetry. Figures S3A and S3B show the heat generation rate after the start of polymerization as a function of time for BIS-crosslinked microgels (A) and BAC-crosslinked microgels (B). BIS-crosslinked microgels show a single sharp peak, which shifts to lower times with increasing concentration of BIS (1 mol% *vs.* 5 mol%), Figure S3A. This peak corresponds to copolymerization of BIS and NIPAm, and the shift is due to a faster polymerization rate of BIS with respect to NIPAm. In contrast, BAC-crosslinked microgels show a much broader peak, which splits into two overlapping peaks with increasing the BAC concentration from 1 mol% to 5 mol%, Figure S3B. Since the polymerization rate of BAC is higher compared to NIPAm, the first peak can be assigned to preferential homopolymerization of BAC, whereas the broad second peak likely corresponds to copolymerization of BAC and NIPAm. Significant broadening of the heat generation rate peak in BAC-crosslinked microgels compared to the BIS crosslinked microgels can be assigned to side-reactions of the S-S group. Such side-reactions can lead to transient formation of (more stable) S· radicals, which might have a slower chain propagation rate or earlier termination of a growing chain. Indeed, the content of S-S groups in the final microgels is systematically lower than the nominal BAC amounts, as shown by the Raman spectroscopy results (Figures S1 and S2).

The completion of the polymerization reaction was verified by following the turbidity of the solutions, Figures S3C and S3D, as well as by simulating the conversion using the iControl RC1e 5.3 software, Figures S3E and S3F. For all microgels, the polymerization was complete within 60 min after adding the initiator, *i.e.* no change of either turbidity or simulated conversion was observed.

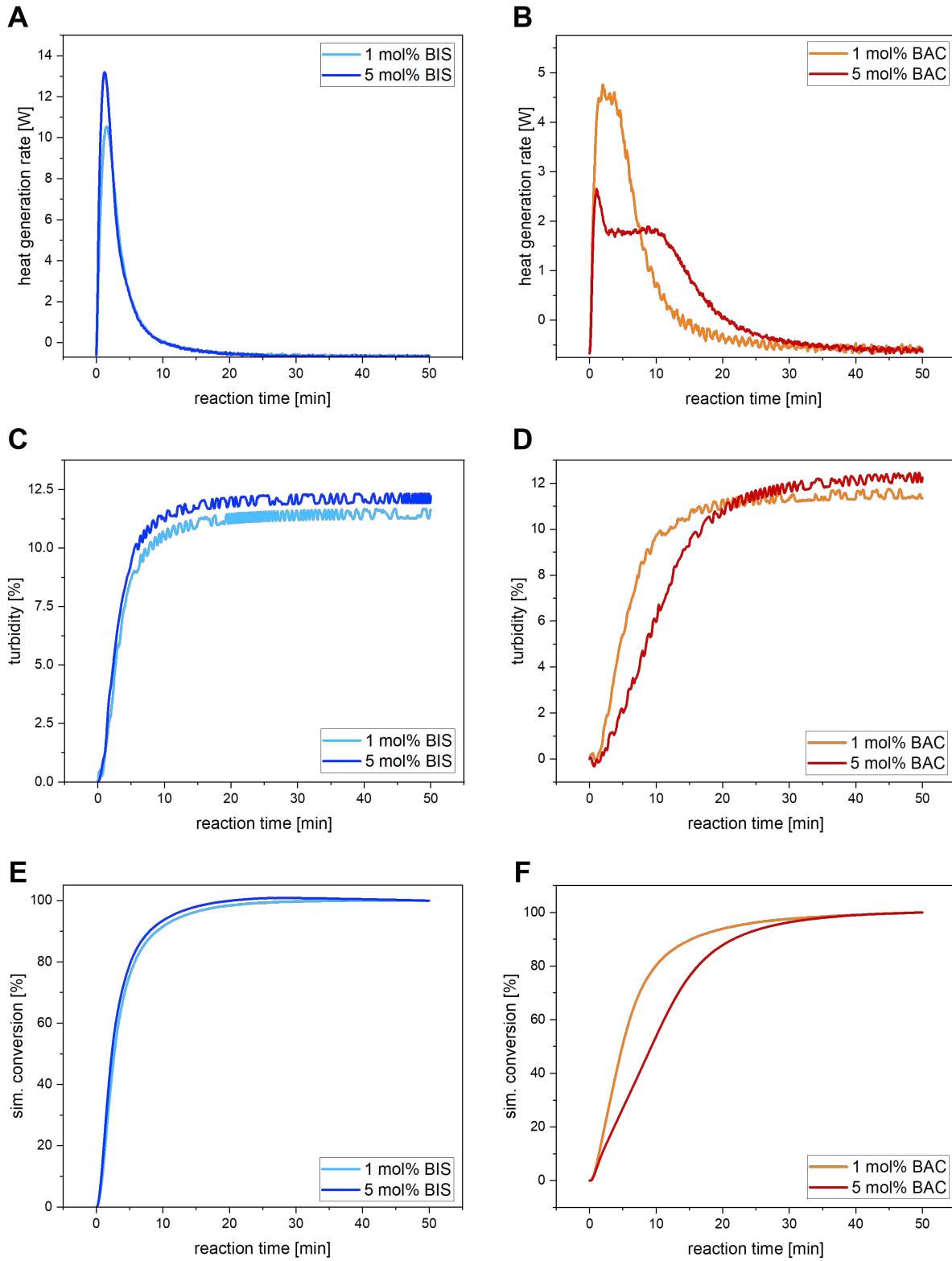


Figure S3: Comparison of the microgel synthesis of pNIPAm/BIS and pNIPAm/BAC microgels initiated with the redox initiation system of APS/TEMED with various crosslinker concentrations of 1 and 5 mol% using in-line reaction calorimetry. Heat generation rate of (A) BIS-crosslinked, and (B) BAC-crosslinked; turbidity of (C) BIS-crosslinked, and (D) BAC-crosslinked; related simulated conversion of (E) BIS-crosslinked, and (F) BAC-crosslinked microgels.

S4. Influence of the BAC Crosslinker on the Swelling Degree

The swelling degrees for BAC-1 and BAC-5 microgels (Table 1, Main Manuscript) are significantly lower than what is expected for pNIPAm microgels with similar amounts of crosslinker.¹ This gives further evidence that part of the BAC crosslinker was consumed in side-reactions, resulting in formation of permanent crosslinks (C-S bonds)² and a higher actual number of crosslinks than expected.

However, the difference in swelling between BIS-1 and BAC-1 microgels cannot be explained only by the increase of the number of crosslinks due to S-S bond dissociation. If we consider that every dissociated S-S crosslink produces two C-S crosslinks and that 0.3 mol% of the S-S bonds remain in the microgels (based on Raman spectroscopy data), then the real number of crosslinks should be:

$$x = (1 \text{ mol\%} - 0.3 \text{ mol\%}) \cdot 2 + 0.3 \text{ mol\%} = 1.7 \text{ mol\%}. \quad (\text{S1})$$

Although the real number of crosslinks is then 70% higher than their nominal number, it is still relatively low and is not sufficient to explain the low swelling degree. Indeed, the swelling degree of BAC-1 microgels, $\alpha_{\text{BAC-1}} = 1.92 \pm 0.02$, is lower than that of the BIS-5 microgels, $\alpha_{\text{BIS-5}} = 2.11 \pm 0.04$, which contain 5 mol% of crosslinks. Other reasons, such as the high hydrophobicity of BAC and a different distribution of crosslinks (network topology), must also contribute to the low swelling degree of BAC-crosslinked microgels.

S5. Additional Scattering Data and Fit Parameters (DLS, SLS, SAXS)

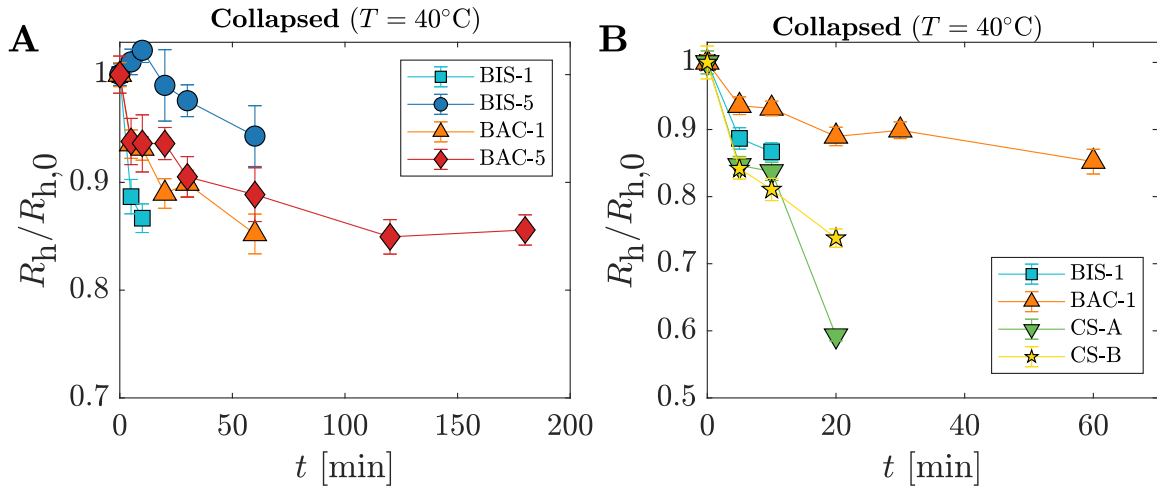


Figure S4: Normalized hydrodynamic radii of the microgels in collapsed state $R_h/R_{h,0}(T = 40^\circ\text{C})$ for: (A) simple microgels and (B) hybrid core-shell microgels.

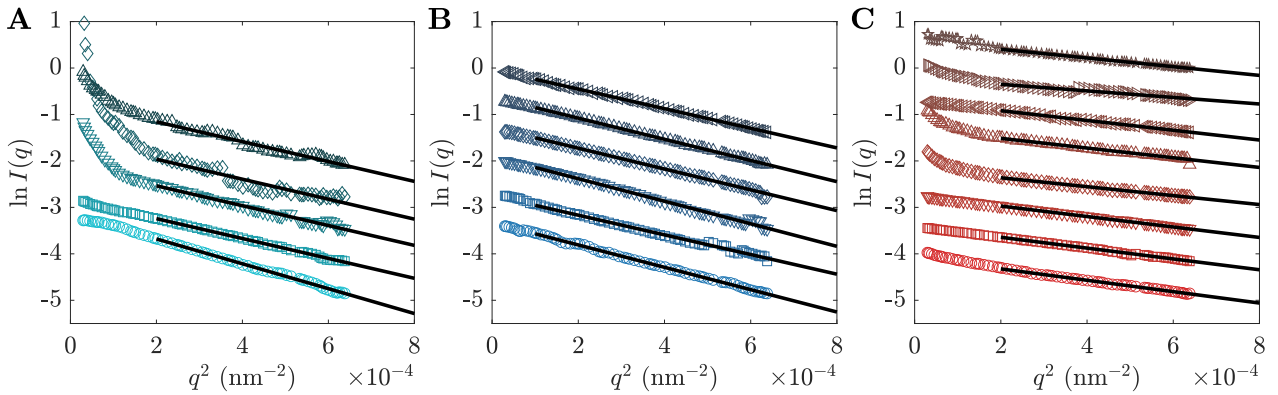


Figure S5: Guinier plots from SLS after different ultrasonication times t for: (A) BIS-1 microgels after 0 min, 5 min, 10 min, 30 min, 60 min ultrasonication (from bottom to top); (B) BIS-5 microgels after 0 min, 5 min, 10 min, 20 min, 30 min, 60 min ultrasonication (from bottom to top); (C) BAC-5 microgels after 0 min, 5 min, 10 min, 20 min, 30 min, 60 min, 120 min, 180 min ultrasonication (from bottom to top). The curves are shifted along the y -axis for clarity. Black solid lines correspond to linear fits.

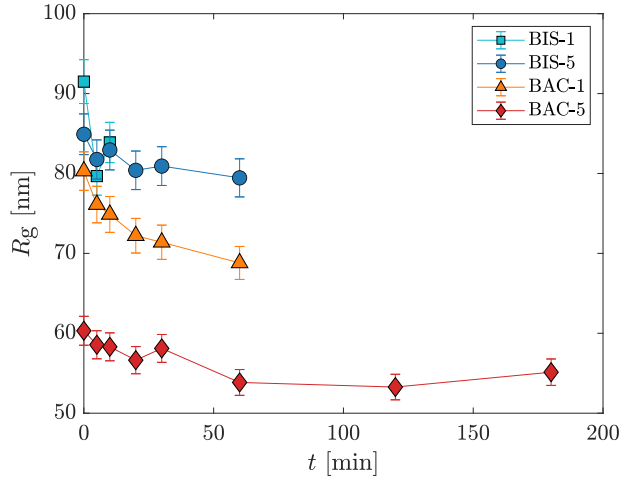


Figure S6: Radii of gyration R_g for the simple microgels *vs.* ultrasonication time t .

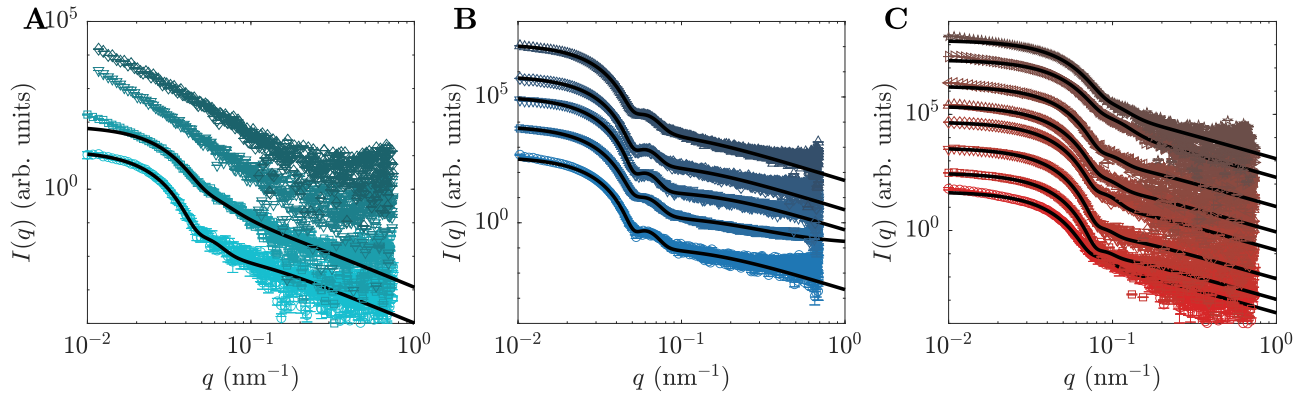


Figure S7: SAXS intensities $I(q)$ *vs.* scattering vector q after different ultrasonication times t for: (A) BIS-1 microgels after 0 min, 5 min, 10 min, 20 min ultrasonication (from bottom to top); (B) BIS-5 microgels after 0 min, 5 min, 10 min, 20 min, 30 min ultrasonication (from bottom to top); (C) BAC-5 microgels after 0 min, 5 min, 10 min, 20 min, 30 min, 60 min, 120 min, 180 min ultrasonication (from bottom to top). The curves are shifted along the y -axis for clarity. Black solid lines correspond to fits using the fuzzy sphere model.

Table S6: Fit parameters of the fuzzy sphere form factor model obtained for the simple microgels (SAXS data) after different ultrasonication times t .

Microgel	t	R [nm]	R_c [nm]	2σ [nm]	p [%]	ξ [nm]
BIS-1	0	130 ± 6	42 ± 2	87 ± 4	17 ± 3	12 ± 2
	5	83 ± 4	50 ± 2	33 ± 2	30 ± 5	15 ± 2
BAC-1	0	121 ± 6	33 ± 2	88 ± 4	10 ± 1	15 ± 2
	5	113 ± 6	40 ± 2	72 ± 4	12 ± 2	12 ± 2
	10	119 ± 6	31 ± 2	88 ± 4	11 ± 2	14 ± 2
	20	110 ± 6	36 ± 2	74 ± 4	12 ± 2	15 ± 2
	30	85 ± 4	56 ± 3	29 ± 1	22 ± 3	11 ± 2
	60	58 ± 3	50 ± 3	7 ± 1	37 ± 6	16 ± 2
	0	133 ± 7	30 ± 2	103 ± 5	10 ± 1	7 ± 1
BIS-5	5	128 ± 6	35 ± 2	93 ± 5	12 ± 2	6 ± 1
	10	136 ± 7	25 ± 1	110 ± 6	9 ± 1	6 ± 1
	20	134 ± 7	29 ± 1	104 ± 5	10 ± 2	9 ± 1
	30	127 ± 6	36 ± 2	91 ± 5	12 ± 2	10 ± 2
BAC-5	0	91 ± 5	21 ± 1	71 ± 4	14 ± 2	16 ± 2
	5	97 ± 5	0 ± 1	97 ± 5	9 ± 1	13 ± 2
	10	97 ± 5	0 ± 1	97 ± 5	10 ± 2	13 ± 2
	20	90 ± 5	14 ± 1	76 ± 4	13 ± 2	14 ± 2
	30	88 ± 4	10 ± 1	78 ± 4	14 ± 2	15 ± 2
	60	83 ± 4	13 ± 1	70 ± 4	13 ± 2	15 ± 2
	120	66 ± 3	26 ± 1	40 ± 2	21 ± 3	20 ± 3
	180	71 ± 4	16 ± 1	54 ± 3	20 ± 3	20 ± 3

Table S7: Fit parameters of the fuzzy core-shell form factor model obtained for the core-shell microgels (SLS data) after different ultrasonication times t .

Microgel	t	R [nm]	R_c [nm]	$2\sigma_{\text{in}}$ [nm]	w [nm]	$2\sigma_{\text{out}}$ [nm]	$\rho_{\text{shell}}/\rho_{\text{core}}$	p [%]
CS-A	0	350 ± 18	38 ± 2	209 ± 10	58 ± 3	45 ± 2	0.174 ± 0.009	9 ± 1
	5	283 ± 14	73 ± 4	130 ± 6	79 ± 4	2 ± 1	0.188 ± 0.009	10 ± 1
	10	278 ± 14	89 ± 4	86 ± 4	82 ± 4	21 ± 1	0.20 ± 0.01	10 ± 1
	20	267 ± 13	107 ± 5	44 ± 2	101 ± 5	15 ± 1	0.21 ± 0.01	12 ± 2
CS-B	0	235 ± 12	11 ± 1	77 ± 4	11 ± 1	135 ± 7	2.6 ± 0.1	13 ± 2
	5	223 ± 11	18 ± 1	62 ± 3	34 ± 2	110 ± 5	2.0 ± 0.1	13 ± 2
	10	202 ± 10	16 ± 1	71 ± 4	40 ± 2	74 ± 4	2.5 ± 0.1	16 ± 2
	20	177 ± 9	18 ± 1	85 ± 4	37 ± 2	36 ± 2	3.3 ± 0.2	18 ± 3

S6. Additional Atomic Force Microscopy Data

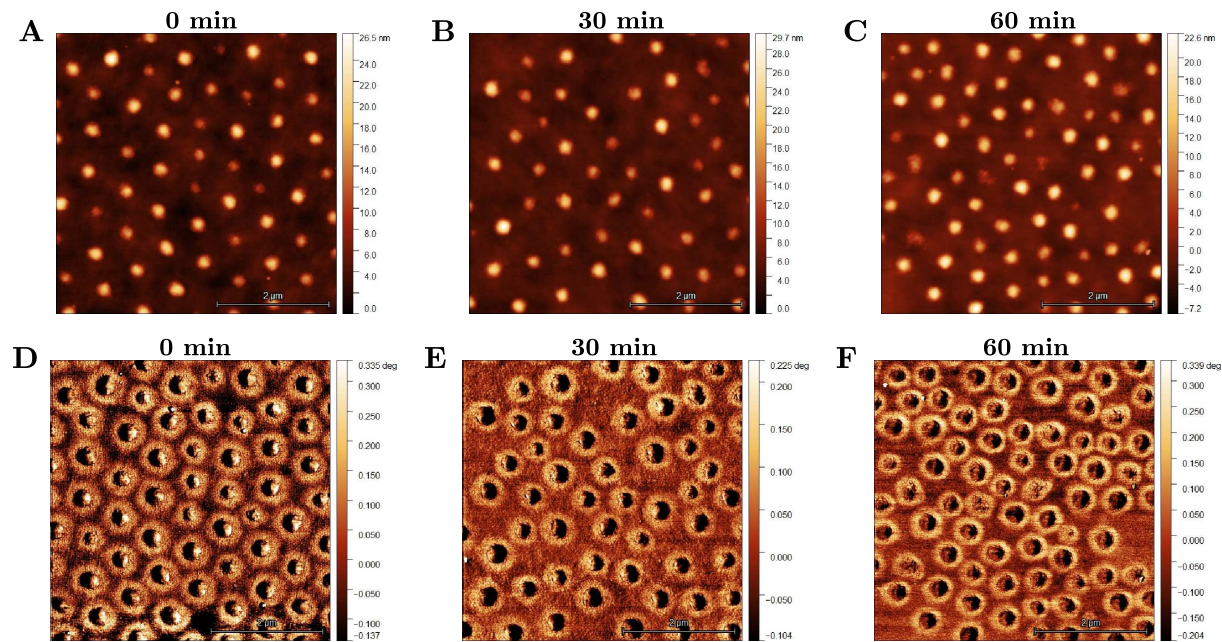


Figure S8: Examples of AFM images of 5% BIS microgels after different ultrasonication times (indicated in the figure). Panels A-C correspond to height images, D-F correspond to phase images. Scale bar is 2 μ m.

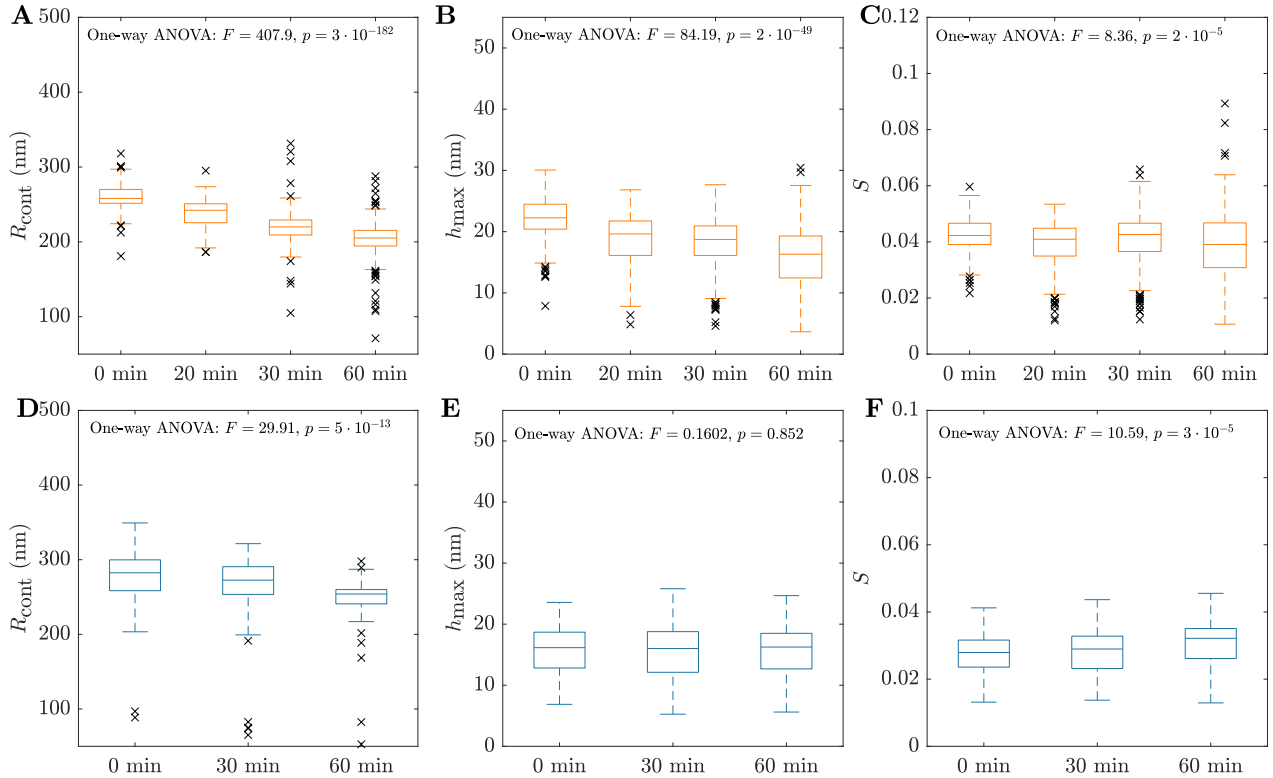


Figure S9: Box plots showing the influence of ultrasonication time t on different parameters obtained by AFM: (A) Contact radii R_{cont} of BAC-1 microgels, (B) Heights h_{max} of BAC-1 microgels, (C) Shape parameter S of BAC-1 microgels, (D) Contact radii R_{cont} of BIS-5 microgels, (E) Heights h_{max} of BIS-5 microgels, (F) Shape parameter S of BIS-5 microgels. Black exes indicates outliers determined as points lying outside of the $\pm 2.7\sigma$ interval.

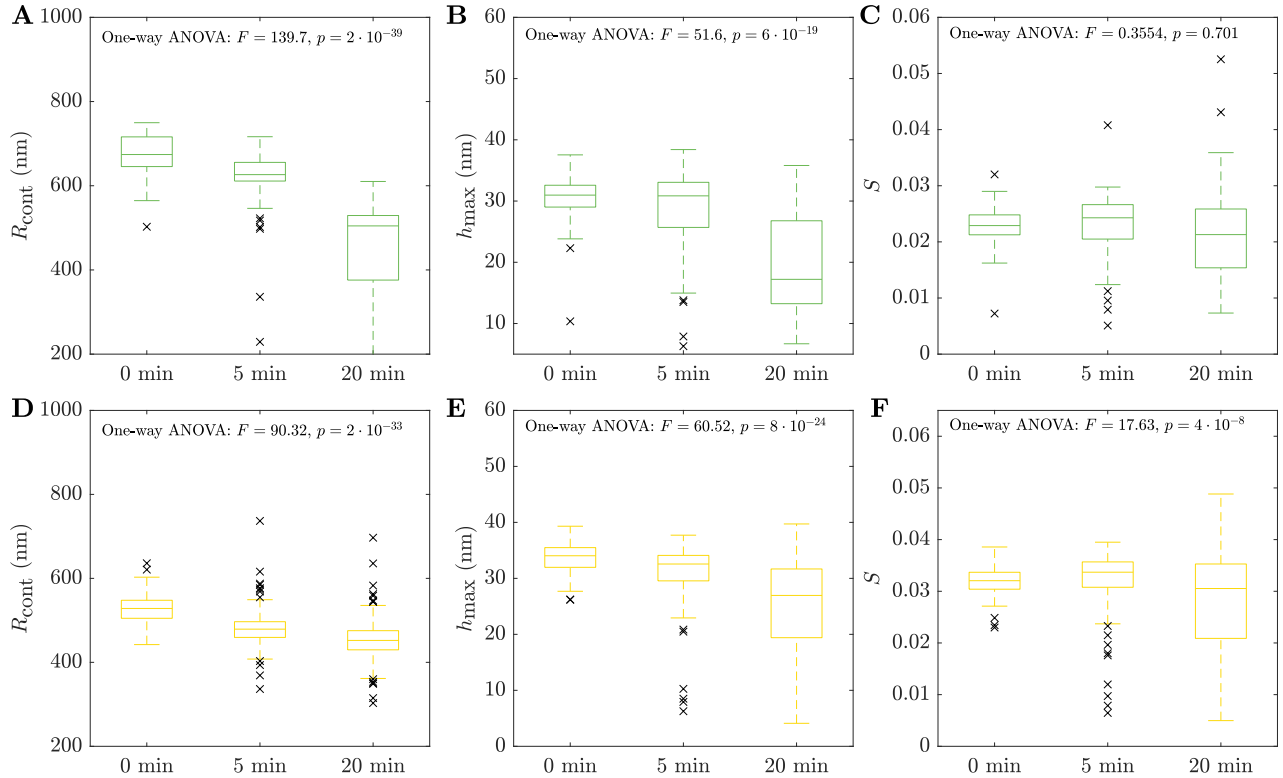


Figure S10: Box plots showing the influence of ultrasonication time t on different parameters obtained by AFM: (A) Contact radii R_{cont} of CS-A microgels, (B) Heights h_{max} of CS-A microgels, (C) Shape parameter S of CS-A microgels, (D) Contact radii R_{cont} of CS-B microgels, (E) Heights h_{max} of CS-B microgels, (F) Shape parameter S of CS-B microgels. Black exes indicates outliers determined as points lying outside of the $\pm 2.7\sigma$ interval.

References

- (1) Lopez, C. G.; Richtering, W. Does Flory–Rehner theory quantitatively describe the swelling of thermoresponsive microgels? *Soft Matter* **2017**, *13*, 8271–8280.
- (2) Gaulding, J. C.; Smith, M. H.; Hyatt, J. S.; Fernandez-Nieves, A.; Lyon, L. A. Reversible inter-and intra-microgel cross-linking using disulfides. *Macromolecules* **2012**, *45*, 39–45.